The Astrophysical Journal Supplement Series, 281:58 (29pp), 2025 December https://doi.org/10.3847/1538-4365/ae1586

Refined M-type Star Catalog from LAMOST DR10: Measurements of Radial Velocities, $T_{\rm eff}$, log g, [M/H], and [α/M]

Shuo Li[1,2], Yin-Bi Li[1,2], A-Li Luo[1,2], Jun-Chao Liang[1,2], You-Fen Wang[1,2], Jing Chen[3,4], Shuo Zhang[5], Mao-Sheng Xiang[1,2], Hugh R. A. Jones[6], Zhong-Rui Bai[1,2], Xiao-Xiao Ma[1,2], Yun-Jin Zhang[1,2], and Hai-Ling Lu[1,2]

[1] CAS Key Laboratory of Optical Astronomy, National Astronomical Observatories, Beijing 100101, People's Republic of China; ybli@bao.ac.cn, lal@nao.cas.cn
[2] University of Chinese Academy of Sciences, Beijing 100049, People's Republic of China
[3] Nanjing Institute of Astronomical Optics & Technology, Chinese Academy of Sciences, Nanjing 210042, People's Republic of China
[4] CAS Key Laboratory of Astronomical Optical & Technology, Nanjing Institute of Astronomical Optics & Technology, Nanjing 210042, People's Republic of China
[5] Department of Astronomy, Tsinghua University, Beijing 100084, People's Republic of China
[6] Centre for Astrophysics Research, University of Hertfordshire, College Lane, Hatfield AL10 9AB, UK

Received 2025 April 7; revised 2025 October 11; accepted 2025 October 13; published 2025 December 9

Abstract

Precise stellar parameters for M-type stars, the Galaxy's most common stellar type, are crucial for numerous studies. In this work, we refined the LAMOST DR10 M-type star catalog through a two-stage process. First, we purified the catalog using techniques including deep learning and color–magnitude diagrams to remove 22,496 non-M spectra, corrected 2078 dwarf/giant classifications, and updated 12,900 radial velocities. This resulted in a cleaner catalog containing 870,518 M-type spectra (820,493 dwarfs, 50,025 giants). Second, applying a label transfer strategy using values from APOGEE DR16 for parameter prediction with a tenfold cross-validated convolutional neural network ensemble architecture, we predicted $T_{\rm eff}$, log g, [M/H], and [α/M] separately for M dwarfs (dMs) and giants (gMs). The average internal errors for dMs/gMs are, respectively, $T_{\rm eff}$ 30/17 K, log g 0.07/0.07 dex, [M/H] 0.07/0.05 dex, and [α/M] 0.02/0.02 dex. Comparison with APOGEE demonstrates external precisions of 34/14 K, 0.12/0.07 dex, 0.09/0.04 dex, and 0.03/0.02 dex for dMs/gMs, which represent precision improvements of over 20% for dMs and over 50% for gMs compared to previous literature results. The catalog is available at doi:10.12149/101668.

Unified Astronomy Thesaurus concepts: M stars (985); Astronomy data analysis (1858); Radial velocity (1332); Fundamental parameters of stars (555); Convolutional neural networks (1938); Catalogs (205)

Materials only available in the online version of record: machine-readable table

1. Introduction

M-type stars are the most common stellar type in the Milky Way, comprising over 70% of the total stellar population (I. N. Reid & J. E. Gizis 1997; J. J. Bochanski et al. 2010; A. Golovin et al. 2023). Based on their mass and evolutionary stage, they can be broadly classified into M dwarfs (dMs) and M giants (gMs; J. D. Kirkpatrick & D. W. J. McCarthy 1991), which exhibit distinct luminosity and radius characteristics in the Hertzsprung–Russell diagram (R. O. Gray & J. C. Corbally 2009). The spectra of M-type stars are characterized by strong molecular absorption bands from species such as TiO, VO, and CaH, which complicate the determination of the continuum and make traditional equivalent-width-based measurement methods difficult to apply. These spectral complexities pose significant challenges for the accurate determination of their atmospheric parameters (A. W. Mann et al. 2015; P. Jofré et al. 2019).

dM stars are hydrogen-burning stars located at the lower end of the main sequence, typically with a mass less than 0.7 $M_\odot$ and an effective temperature ranging from 2400 to 4000 K (J. D. Kirkpatrick et al. 1993; J. Li et al. 2023). They have extremely long lifetimes, far exceeding the Hubble time, making them important tools for tracing the chemical and dynamical history of the Milky Way (G. Laughlin et al. 1997). In recent years, with the advancement of exoplanet detection technologies, dMs have become preferred targets for the search for Earthlike planets due to their small size and low mass (A. L. Shields et al. 2016; D. Kossakowski et al. 2023; Y. N. E. Eschen & M. Kunimoto 2024). Several potentially habitable exoplanets have been discovered orbiting dMs, including systems such as Proxima Centauri, TRAPPIST-1, and LHS 1140 (S. L. Grimm et al. 2018; J. Lillo-Box et al. 2020; J. P. Faria et al. 2022). gMs, on the other hand, are high-luminosity, low-temperature stars, including those at the tip of the red giant branch, asymptotic giant branch stars, and red supergiants (A. I. Boothroyd & I. J. Sackmann 1999; R. Kippenhahn et al. 2013). Due to their high luminosity, gMs are used to trace distant regions and serve as ideal tracers for revealing the accretion and merger events in the Milky Way, especially for studying stellar streams in the Galactic halo, such as the Sagittarius system (R. A. Ibata et al. 1994; J. Li et al. 2016; C. Yang et al. 2019). Therefore, to accurately characterize the exoplanetary physical properties of dMs and study the accretion and merger history of the Milky Way, it is essential to precisely measure the fundamental physical parameters of M-type stars, including effective temperature ($T_{\rm eff}$), surface gravity (log g), and metallicity ([M/H]).

Spectral analysis is a crucial method for obtaining the fundamental parameters of stars, enabling the determination of a star's $T_{\rm eff}$, log g, [M/H], and other physical characteristics. In recent years, several large-scale survey projects have provided abundant observational data for such studies. For example, high-resolution surveys such as the Apache Point Observatory Galactic Evolution Experiment (APOGEE; S. R. Majewski et al. 2017), the Galactic Archaeology with HERMES (G. M. De Silva et al. 2015), the Calar Alto high-Resolution search for dM with Exo-earths with Near-infrared and optical Echelle Spectrographs (CARMENES; A. Quirrenbach et al. 2020), and the Gaia-ESO Survey (G. Gilmore et al. 2012); medium-resolution surveys like the Radial Velocity Experiment (M. Steinmetz et al. 2006) and the Large Sky Area Multi-Object Fiber Spectroscopic Telescope (LAMOST) Medium-Resolution Spectroscopic Survey (C. Liu et al. 2020); and low-resolution surveys such as the Sloan Extension for Galactic Understanding and Exploration (B. Yanny et al. 2009), the LAMOST Experiment for Galactic Understanding and Exploration (L.-C. Deng et al. 2012), and the Gaia BP/RP spectra (F. De Angeli et al. 2023). These survey projects have made invaluable contributions to stellar spectral research, and the massive data sets from these surveys have created an urgent demand for accurate measurements of M-type star parameters, further driving rapid development in related research.

For the problem of stellar parameter determination from high-resolution spectroscopy of M-type stars, early studies primarily relied on traditional model-fitting techniques. For instance, A. S. Rajpurohit et al. (2018) were the first to simultaneously use high-resolution optical and near-infrared spectra observed by CARMENES combined with the BT-Settl models (F. Allard et al. 2011), deriving T_{eff}, log g, and [M/H] for 292 dMs through least-squares fitting, with uncertainties of 100 K, 0.3 dex, and 0.3 dex, respectively. V. M. Passegger et al. (2018, 2019) employed the updated PHOENIX-ACES models (T. O. Husser et al. 2013) and χ^2 minimization methods to determine T_{eff}, log g, and [M/H] for 300 dMs, improving the uncertainties to 51 K, 0.07 dex, and 0.16 dex. E. Marfil et al. (2021) derived atmospheric parameters for 343 dMs based on CARMENES spectra employing the STEPARSYN Bayesian spectral synthesis implementation, combining BT-Settl models with the radiative transfer code `turbospectrum`, and imposed Bayesian priors based on multiband photometric data to avoid any potential degeneracy in the parameter space. In recent years, data-driven methods have rapidly developed. V. M. Passegger et al. (2020) first applied convolutional neural networks (CNNs) trained on synthetic PHOENIX-ACES spectra to directly predict T_{eff}, log g, [M/H], and $v \sin i$ from dM spectra observed by CARMENES, but encountered a significant "synthetic gap" problem, where differences in feature distributions between synthetic and observed spectra led to notable biases in metallicity predictions. To mitigate this issue, A. Bello-García et al. (2023) developed a deep transfer learning approach, utilizing T_{eff} determined from interferometry and [M/H] from FGK + M binaries to fine-tune the internal features of neural networks trained on synthetic PHOENIX-ACES spectra, achieving improvements of 20 K and 0.2 dex in T_{eff} and [M/H] accuracy, respectively, compared to V. M. Passegger et al. (2020). P. Mas-Buitrago et al. (2024) further proposed a feature-based deep transfer learning method that does not require high-quality measurements of parameters involved in the knowledge transfer, effectively alleviating the impact of the "synthetic gap."

However, extending the successful experience of M-type stellar parameter measurements from high-resolution spectroscopy to low-resolution large-scale surveys faces even more formidable challenges. Compared to G-type stars, the dominance of molecular lines in M-type stellar atmospheres results in more pronounced discrepancies between theoretical models and actual observations. In the optical band, only about half of the spectral lines have accurately determined laboratory parameters (R. L. Kurucz 2014), and the abundance of molecular features in cool stellar atmospheres further increases the complexity of modeling (P. Jofré et al. 2019). These theory–observation inconsistencies become even more pronounced in low-resolution spectra, directly compromising the accuracy of parameter measurements. For instance, the LAMOST Stellar Parameter Pipeline for M-type stars (LASPM) was developed by B. Du et al. (2021), which finds the best-matching templates in the BT-Settl synthetic spectral library for each observed spectrum and then minimizes χ^2 through a linear combination of the five best-matching templates to derive atmospheric parameters, exhibits significant systematic deviations when compared to high-resolution APOGEE results, such as an overestimation of surface gravity by approximately 0.63 dex and an underestimation of metallicity by about 0.25 dex, along with considerable dispersion exceeding 0.2 dex for both surface gravity and metallicity. These discrepancies highlight the limitations of applying theoretical models to the measurement of M-type stellar parameters from low-resolution spectroscopy.

To address the challenges of low-resolution M-type spectral analysis, researchers have explored various approaches. J. Li et al. (2021) employed the Stellar Label Machine (SLAM) model to transfer the high-precision labels from APOGEE DR16 to LAMOST spectra, measuring T_{eff} and [M/H] for approximately 300,000 dMs. D. Qiu et al. (2023) applied the SLAM method to gMs, deriving T_{eff}, log g, [M/H], and alpha element abundance ([α/M]) for 43,972 gM spectra. M.-Y. Ding et al. (2022) used the MILES (J. Falcón-Barroso et al. 2011) empirical spectral library to determine T_{eff}, log g, and [M/H] for 763,136 spectra of M-type stars in LAMOST DR8. J.-C. Liang et al. (2024) proposed a spectral emulator approach using the MaStar observed spectral library to measure T_{eff}, log g, [M/H], and [α/M] for O- to M-type stars in LAMOST DR10. B. Du et al. (2024) improved the accuracy of LASPM parameter measurements by constructing a more self-consistent M-type star spectral library. S. Zhang et al. (2025) applied the Cycle-StarNet technique to significantly reduce the discrepancies between theoretical and observed spectra and derived T_{eff}, log g, and [M/H] for 507,513 dM spectra in LAMOST DR10. Most of these studies adopted parameter inference methods based on iterative optimization. Compared to APOGEE results, the dispersion in log g and [M/H] for gM is generally larger than that for dM, typically in the range of 0.2–0.32 dex. Therefore, further improving the measurement precision of log g and [M/H] for M-type stars, particularly for gM, remains a key focus for future research.

This work adopted a "label transfer + parameter prediction" strategy to estimate M-type star parameters, where a neural network model is trained using LAMOST spectra with high-precision parameters from APOGEE and then applied to other LAMOST spectra. This approach effectively reduces systematic errors introduced by the "synthetic gap" (V. M. Passegger et al. 2020), relative to directly applying synthetic-trained models to observed spectra. Compared to the iterative optimization-based parameter inference methods commonly used in previous studies, the "parameter prediction" method employed in this work improves both efficiency and accuracy in parameter estimation. The structure of this paper is as follows. Section 2 describes the data used in this work. Section 3 introduces the workflow, spectral preprocessing, CNN framework, and technical details. Section 4 presents the construction of the recommended catalog and a comparative analysis of the stellar parameters provided in this work with those from previous studies. The conclusions are summarized in Section 5.

2. Data

2.1. LAMOST

LAMOST (also called the Guo Shou Jing Telescope), located in the Xinglong station of the National Astronomical Observatories, Chinese Academy of Sciences, is a special reflecting Schmidt telescope with 4000 fibers in a field of view of 20 deg^2 in the sky (S.-G. Wang et al. 1996; D.-Q. Su & X.-Q. Cui 2004; X.-Q. Cui et al. 2012). LAMOST is dedicated to a spectral survey of celestial objects over the entire available northern sky, providing a large number of medium- ($R \sim 7500$) and low-resolution ($R \sim 1800$) spectra (L.-C. Deng et al. 2012; G. Zhao et al. 2012). The regular survey of LAMOST started in 2012 September (A. L. Luo et al. 2015), and as of DR10 v1.0,[7] LAMOST has published over 11.8 million low-resolution spectra with a wavelength range of 3700–9000 Å, which includes about 11.4 million stellar spectra. Additionally, LAMOST DR10 v1.0 also provides a catalog of M-type stars, which contains 818,676 dM spectra, 53,481 gM spectra, and 3977 M subdwarf (sdM) spectra, and all of this work was conducted based on this catalog.

2.2. Gaia

The European Space Agency's (ESA) Gaia mission (Gaia Collaboration et al. 2016), initiated in 2013, has progressed to its third data release (Gaia DR3). The Gaia satellite was equipped with three main instruments: the astrometric instrument to collect images in the broad G band (330–1050 nm), the blue BP and red RP prism photometers for low-resolution spectra, and the radial velocity spectrometer (RVS) for measuring radial velocities (RVs; Gaia Collaboration et al. 2023b). Gaia DR3 provides G-band photometry for 1.8 billion sources, parallax, proper motion, G_{BP} and G_{RP} for 1.5 billion sources, and RV measurements for 33 million bright stars ($G_{\mathrm{RVS}} < 14$, $3100 < T_{\mathrm{eff}} < 14{,}500$ K) (M. Fouesneau et al. 2023). Additionally, it also provides the renormalized unit weight error (RUWE; L. Lindegren et al. 2018), a metric designed to assess the goodness of the astrometric fit.

2.3. APOGEE

The Sloan Digital Sky Survey (SDSS; D. G. York et al. 2000) started observations in 1998 and is now in its fourth phase (SDSS-IV; M. R. Blanton et al. 2017). The collected data of SDSS-IV includes optical images of most of the northern high Galactic latitude sky as well as optical and near-infrared spectroscopy of over 3.5 million targets, and these observations all used the 2.5 m Sloan Foundation Telescope at Apache Point Observatory (J. E. Gunn et al. 2006). APOGEE-2 is a key project of SDSS-IV, and a major near-infrared (15140–16940 Å) spectroscopic survey to investigate the composition and dynamics of stars in the Galaxy, based on multiplexed high-resolution ($R \sim 22{,}500$) spectrographs. APOGEE DR16[8] observed spectra for about 430,000 stars of both the northern and southern sky (H. Jönsson et al. 2020), and provided atmospheric parameters (T_{eff}, $\log g$, [M/H]) and chemical abundances (such as [α/M], [C/M], and [N/M]) using the APOGEE Stellar Parameter and Chemical Abundance Pipeline (ASPCAP; A. E. García Pérez et al. 2016), which was developed for the automated analysis of observed spectra.

2.4. Spectral Templates

In this work, when employing the template-matching (TM) method to measure the RVs of M-type stars, spectral templates from J. Zhong et al. (2016) and the LAMOST spectral analysis pipeline (LAMOST 1D pipeline; A. L. Luo et al. 2012) were used. J. Zhong et al. (2015a) and J. Zhong et al. (2015b) detailed the development of templates for dM and gM stars, respectively. The dwarf star templates are derived from the SDSS DR7 M-type star catalog published by A. A. West et al. (2011), while the giant star templates were selected from M-type star spectra of LAMOST DR1. Zhong et al.'s catalog contains 223 M-type star templates, including only seven giant star templates covering a wavelength range of 4700–9000 Å. The LAMOST 1D pipeline provides 10 dwarf (dM0–dM9) and 10 giant (gM0–gM9) templates, with a wavelength range of 3865–8997 Å. Due to the limited number of giant templates in Zhong et al.'s collection, which are significantly fewer than the dwarf templates and lack late-type giants beyond M6, this work combined Zhong et al.'s templates with all 10 giant templates from the LAMOST 1D pipeline for measuring RVs. The resolution of the M-type star templates from both J. Zhong et al. (2016) and LAMOST is ∼1800. Spectral preprocessing, such as wavelength range alignment, was conducted during the merging of the templates, as detailed in Section 3.2.

3. Method

3.1. Workflow

In the M-type star catalog of LAMOST DR10 (we call M_Catalog_V0 hereafter), there are a total of 876,134 spectra, including 822,653 dwarf star spectra and 53,481 giant star spectra. However, the classification results from the LAMOST 1D pipeline are not entirely accurate, with some non-M-type stars mixed in, and errors in the classification between dwarf and giant stars for some spectra. Additionally, the RVs provided by LAMOST also contain errors in some cases. To obtain a more reliable M-type star catalog (called the recommended catalog hereafter), with more accurate spectral type, dwarf/giant classification, RV, and stellar parameter measurements, we designed a specific procedure to achieve as much purity as possible.

To construct the recommended catalog, we designed four modules: the spectral classification module (SCM), the dwarf/giant classification module (DGCM), the RV measurement module (RVMM), and the stellar parameter measurement module (SPMM). In the SCM, DGCM, and SPMM modules, we trained multiple one-dimensional (1D) CNN (Z.-P. Zheng et al. 2020) models using PyTorch (A. Paszke et al. 2019) to classify spectra and measure stellar parameters of LAMOST

---

[7] Data available at https://www.lamost.org/dr10/v1.0/. We chose to use DR10 v1.0 rather than the later-released DR10 v2.0 because: (1) our analysis was initiated using v1.0, and was already in its final stages when v2.0 became available, and (2) v1.0 contains a larger data set that enables us to construct a larger M-type star catalog.

[8] To ensure complete parameter coverage, we used APOGEE DR16 rather than DR17, as the latter excludes [M/H] and [α/M] values for dM stars with T_{eff} below 3500 K due to known systematic issues (Abdurro'uf et al. 2022).

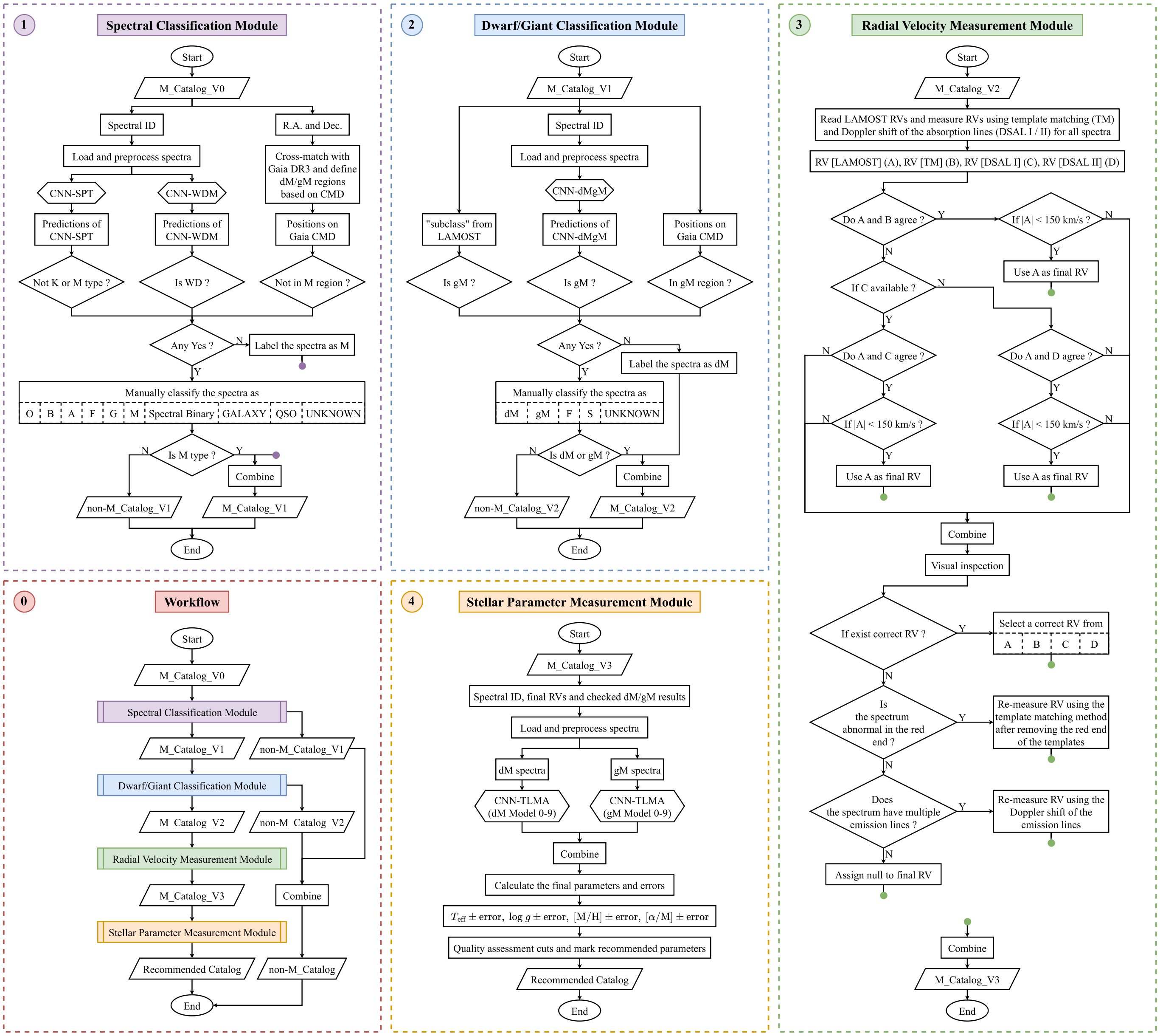

Figure 1. Workflow diagram. Panel (0) illustrates the workflow for constructing a purer M-type star catalog, which consists of four modules: the SCM, the DGCM, the RVMM, and the SPMM. These modules are designed for spectral classification, dM and gM classification, RV measurement, and stellar parameter estimation, respectively. Panels (1)–(4) present the flowcharts of these four modules. It is important to note that in panels (1) and (3), purple and green dots are used to indicate breakpoints to avoid overlap between connecting lines. In reality, these breakpoints lie along the same connecting line.

M-type stars. In the SCM, we trained a model for spectral classification of OB (since the number of O- and B-type stars is relatively small, we combine them into a single class, abbreviated as OB), A, F, G, K, M, GALAXY, and QSO (CNN-SPT), as well as a model for white dwarf (WD) and M spectra classification (CNN-WDM). In the DGCM, we developed a model for classifying dM and gM spectra (CNN-dMgM) to correct potential luminosity classification errors in LAMOST M-type stars. In the RVMM, we adopted two methods to measure the RVs of M-type stars: the TM and Doppler shift methods. In the SPMM, we trained models to measure parameters of $T_{\rm eff}$, log g, [M/H], [α/M] (CNN-TLMA), aiming to address issues in parameter measurements of LAMOST M-type stars and provide additional stellar parameters.

Figure 1 shows the workflow (panel (0)) of this work and the detailed procedures (panels (1)–(4)) of the four modules, where each module progressively enriches the output catalog by incorporating newly derived useful information generated through the processing. First, the SCM refined the spectral classification by identifying and removing non-M-type stars from M_Catalog_V0. The confirmed M-type stars were stored in M_Catalog_V1, while the rejected non-M-type stars were collected in non-M_Catalog_V1. Second, the DGCM processed M_Catalog_V1 to improve the dwarf/giant classification accuracy. During this step, additional non-M-type stars that were missed by SCM were identified and stored in non-M_Catalog_V2, while the remaining M-type stars with updated dM/gM classifications were saved as M_Catalog_V2. Third, the RVMM processed M_Catalog_V2 to provide corrected RV measurements, updating the catalog to M_Catalog_V3. Finally, the SPMM predicted stellar parameters and corresponding errors based on the updated RV results in

M_Catalog_V3, generating the recommended catalog. Since no additional non-M-type stars were removed after the DGCM stage, the non-M-type stars from non-M_Catalog_V1 and non-M_Catalog_V2 were combined to form the comprehensive non-M_Catalog as a byproduct of this purification process. After passing through these four modules, 5616 non-M-type spectra were removed, the dM/gM classification for 2078 spectra was corrected, RVs for 12,900 spectra were revised, and the parameters $T_{\rm eff}$, log g, [M/H], and [α/M] were measured for 870,518 spectra.

It should be noted that we previously identified 16,880 non-M-type spectra in the DR8 M-type star catalog and reclassified them. According to the data release requirements at that time, subsequent data releases after DR8 used our classification results to update these spectra to the correct types, and spectra classified as UNKNOWN due to low signal-to-noise ratio (S/N) or data quality issues were no longer included in releases after DR8. Therefore, the final non-M_Catalog does not include the 16,880 spectra whose classifications had already been updated in the LAMOST official releases, and it includes only the 5616 non-M-type spectra newly identified from the ninth and tenth observing years. Our refined M-type star catalog—the recommended catalog—also excludes all of these identified non-M-type spectra.

3.2. Spectral Preprocessing

As described in Section 3.1, we designed four modules in this work: SCM, DGCM, RVMM, SPMM, and performed preprocessing on the input spectra. Below are the preprocessing steps involved in this work, which vary across each module and will be detailed further in Section 3.4.

1. Remove the flux points corresponding to the `ormask`[9] value of nonzero.
2. Shift the spectra to the rest frame.
3. Linearly interpolate the spectra to have a wavelength interval of 1 Å.
4. Reset the wavelength range of the spectra to
    a. 3900–8899 Å.
    b. 4700–8899 Å.
5. Z-score normalization,

$$\frac{x - x_\mu}{x_\sigma}.$$

In the SCM and DGCM modules, the preprocessing steps used for the CNN-SPT, CNN-WDM, and CNN-dMgM models include operations 1, 3, 4a, and 5. In the RVMM module, when measuring RVs using the TM method, only step 1 was used for preprocessing the observed spectra, while steps 3, 4b, and 5 were used to preprocess the template spectra. This ensures that both Zhong et al.'s templates and the 10 templates of the LAMOST 1D pipeline (mentioned in Section 2.4) have consistent wavelength ranges and flux scales. For measuring RVs using the Doppler shift method, no preprocessing was performed on the observed spectra. In the SPMM module, the preprocessing steps used for the CNN-TLMA model include 1, 2, 3, 4a, and 5, where step 2 used RVs from the RVMM module.

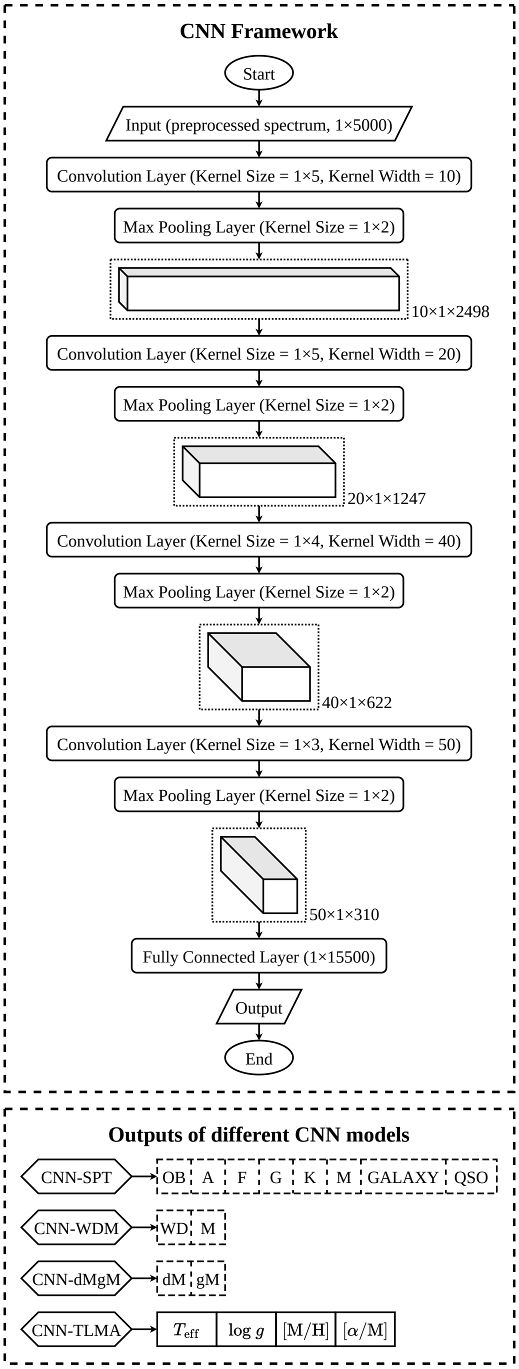

Figure 2. The CNN network architecture used in this work and the outputs of the different CNN models. The CNN-SPT model is used for spectral type classification, the CNN-WDM model is used for WD and M-type star classification, the CNN-dMgM model is used for dM and gM classification, and the CNN-TLMA model is used for measuring the stellar parameters. It should be noted that the outputs of CNN-SPT, CNN-WDM, and CNN-dMgM are the probabilities of each type, while the output of CNN-TLMA consists of four stellar parameters.

3.3. CNN Framework

As described in Section 3.1, we designed four CNN models in this work: CNN-SPT, CNN-WDM, CNN-dMgM, and CNN-TLMA, where the first three are classification models, and the last one is a regression model. The common feature of all four models is that they share the same network architecture, as shown in Figure 2, which consists of four convolutional layers, four

---

[9] The `ormask` is a decimal integer represented by a six-bit binary number for each wavelength of the LAMOST spectrum. A value of 0 indicates that no issues were encountered in any exposure during the spectrum reduction process, while a nonzero value means that at least one exposure encountered issues during the spectrum reduction process for that wavelength.

max-pooling layers, and one fully connected layer. The activation function used in each layer was the rectified linear unit, the optimizer was Adam (D. P. Kingma & J. Ba 2014), the batch size was set to 128, and the initial learning rate was set to 0.001. An adaptive learning rate adjustment method was used to help the model escape local minima, and training was terminated early to prevent overfitting when the validation loss reached its minimum. The key differences between the models lie in the labels and the loss functions. For the classification models (CNN-SPT, CNN-WDM, CNN-dMgM), the labels were one-hot encoded, and the loss function used was cross entropy. The softmax function was applied to convert the model's output into class probabilities, and the class with the highest probability was taken as the predicted spectral type. In contrast, for the regression model (CNN-TLMA), the labels were Z-score normalized to eliminate scale differences between the labels. The loss function used was mean squared error, and the model's output was denormalized to return the predicted stellar parameters on their original scale.

3.4. Module Analysis

3.4.1. SCM

To identify non-M-type spectra from M_Catalog_V0 as thoroughly as possible, we combined the prediction results from CNN-SPT and CNN-WDM models, as well as the positions on the Gaia color–magnitude diagram (CMD), to select non-M-type candidates discussed later. First, we trained two CNN models—CNN-SPT and CNN-WDM—to classify the spectra in the M_Catalog_V0. Both the training data and labels are from the LAMOST DR10 LRS Catalogs.[10] For simplicity, we will refer to these catalogs by their names without the prefix "LAMOST LRS" in subsequent descriptions. The spectral types include OB, GALAXY, QSO from the "General Catalog," A, F, G, K from the "Stellar Parameter Catalog of A, F, G, and K Stars," M from the "Catalog of gM, dM, and sdM Stars" (i.e., M_Catalog_V0), and WD from the "Catalog of White Dwarf Stars." To ensure the reliability of the training data and labels, we excluded spectra with S/N_max $<$ 5, where S/N_max = max(S/N_u, S/N_g, S/N_r, S/N_i, S/N_z) represents the maximum S/N across the u, g, r, i, and z bands. This criterion ensures that each retained spectrum has at least one band with sufficient spectral quality for analysis. Such low-S/N_max spectra account for only 2.90% of all LAMOST-released spectra. Additionally, we cross-referenced the "golden sample of OBA and FGKM stars" from Gaia Collaboration et al. (2023a), the "good QSO and galaxy candidates" from Gaia Collaboration et al. (2023b), and the SIMBAD astronomical database (M. Wenger et al. 2000) using TOPCAT (M. B. Taylor 2005) software and a 3″ matching radius. All subsequent catalog crossmatching was performed using the same tool and matching radius. We filtered the labels based on both the sample size and the consistency of classification results. From the filtered samples, we randomly selected 30,000 spectra from each category as the final training data. The training and validation sets were split in a 3:1 ratio. Since the number of OB and WD spectra was insufficient (8279 and 7094, respectively), we used weighted loss calculation to address the data imbalance issue. The weight values assigned to OB and WD were 3.62 and 4.23, respectively, while all other categories were assigned a weight of 1. Figures 3 and 4 show the confusion matrices for CNN-SPT and CNN-WDM on the validation set, with average accuracies of 99.18% and 99.68%, respectively. If WD is included as an output type in the CNN-SPT model, the confusion matrix on the validation set, as shown in Figure 5, results in an average accuracy of only 98.29%, with the accuracy for WD dropping from 99.69% to 95.94%. Therefore, we adopted a two-model approach for spectral type classification. The CNN-SPT model classifies the spectra from M_Catalog_V0 into nine categories: OB, A, F, G, K, M, GALAXY, QSO, with 3327 spectra predicted as non-K or non-M types. The CNN-WDM model classifies the spectra into two categories: WD and M, with 3809 spectra predicted as WD. It is important to emphasize that although the spectral types of inputs to CNN-SPT and CNN-WDM may potentially fall outside the predefined output categories of these models, we conduct rigorous manual verification of all identified non-M-type candidate spectra to ensure the reliability of our classification methodology.

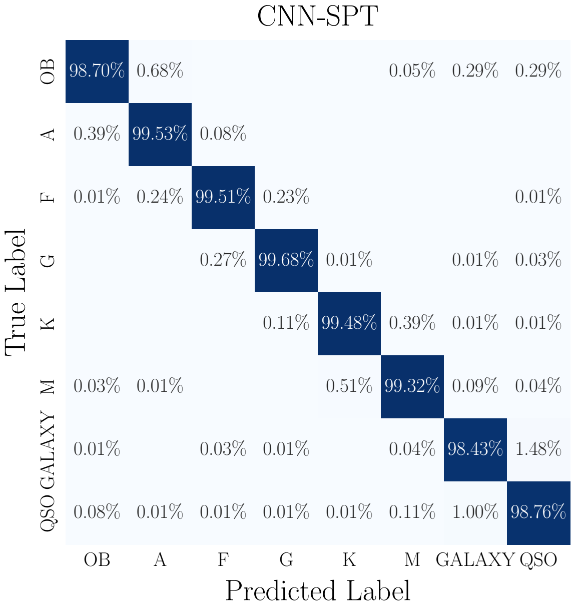

Figure 3. Confusion matrix of the CNN-SPT model on the validation set.

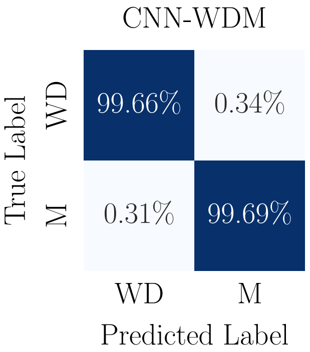

Figure 4. Confusion matrix of the CNN-WDM model on the validation set.

Next, we filtered samples not in the dM or gM regions on the Gaia CMD. To obtain Gaia's color and magnitude data, we crossmatched M_Catalog_V0 with Gaia DR3, yielding 658,857 sources and 866,842 spectra. Figure 6 shows the extinction-corrected Gaia CMD, where the absolute magnitude

---

[10] https://www.lamost.org/dr10/v1.0/catalog

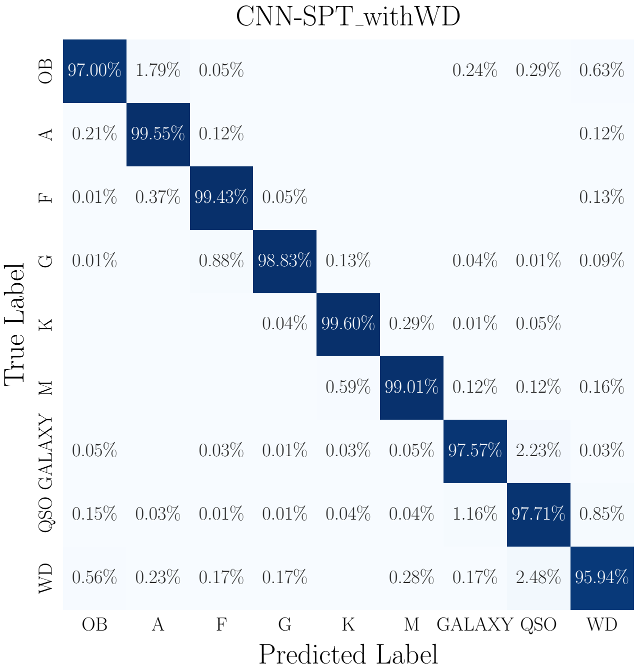

	OB	A	F	G	K	M	GALAXY	QSO	WD
OB	97.00%	1.79%	0.05%				0.24%	0.29%	0.63%
A	0.21%	99.55%	0.12%						0.12%
F	0.01%	0.37%	99.43%	0.05%					0.13%
G	0.01%		0.88%	98.83%	0.13%		0.04%	0.01%	0.09%
K				0.04%	99.60%	0.29%	0.01%	0.05%	
M					0.59%	99.01%	0.12%	0.12%	0.16%
GALAXY	0.05%		0.03%	0.01%	0.03%	0.05%	97.57%	2.23%	0.03%
QSO	0.15%	0.03%	0.01%	0.01%	0.04%	0.04%	1.16%	97.71%	0.85%
WD	0.56%	0.23%	0.17%	0.17%		0.28%	0.17%	2.48%	95.94%

Figure 5. Confusion matrix of the CNN-SPT model with WD type included on the validation set.

M_G for each star is calculated using the following formula:

$$M_{\rm G} = {\rm G} - 5\,{\rm lg}(d) + 5 - A_{\rm G} \qquad (1)$$

where the distance d is taken from C. A. L. Bailer-Jones et al. (2021)'s `r_med_geo`, the reddening $E(B-V)$ is determined from the 3D dust map Bayestar19 (G. M. Green et al. 2019), and the extinction coefficient is from L. Casagrande & D. A. VandenBerg (2018). We used the criteria mentioned in Section 3.1 of J. Li et al. (2021) to select spectra with reliable Gaia colors $G_{\rm BP} - G_{\rm RP}$ and apparent magnitudes G, and the selection criteria are as follows:

1. `parallax_over_error` > 5.
2. `phot_g_mean_flux_over_error` > 20.
3. `phot_bp_mean_flux_over_error` > 20.
4. `phot_rp_mean_flux_over_error` > 20.
5. `ruwe` < 1.4.

Based on Figure 1 in J. Li et al. (2021), we outlined the dM region in quadrilateral shapes in Figure 6, and a line was empirically used to separate the gM region. A total of 7886 spectra in Figure 6 fall outside the dM and gM regions. We combined three sets of spectra: those predicted by CNN-SPT as non-K or non-M, those predicted by CNN-WDM as non-M, and those not in the dM or gM regions on the Gaia CMD, resulting in 13,436 spectra for visual inspection. The results of the visual inspection are shown in Table 1, with 3906 non-M-type spectra identified and stored in the non-M_Catalog_V1. The remaining 9530 spectra classified as M-type and the 862,698 spectra directly marked as M were combined into a total of 872,228 spectra, which were stored in M_Catalog_V1. As mentioned in Section 3.1, we also corrected the types of 16,880 non-M-type spectra found in DR8, and the updated spectral types are shown in Table 2. Figure 7 presents examples of the non-M-type spectra we identified, and it also shows the changes in their classification results. Here, emission-line (EM) stars are non-M-type stars with emission lines in their spectra.

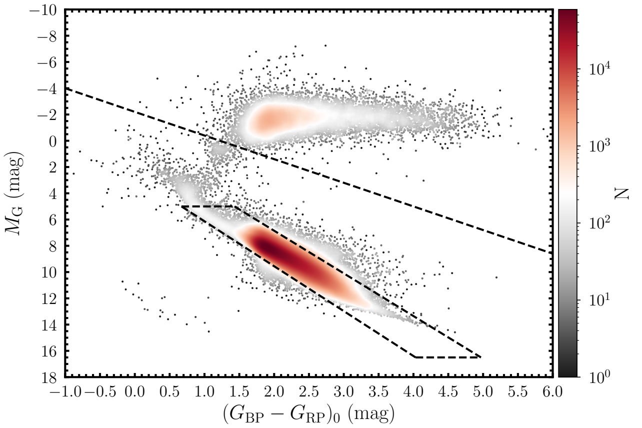

Figure 6. The CMD of the M-type star catalog (M_Catalog_V0) of LAMOST DR10. The Gaia absolute magnitude and color used in this diagram are extinction-corrected values. The quadrilateral enclosed by the dashed line marks the dM region, with the coordinates of the four vertices being (0.7, 5), (1.4, 5), (4, 16.5), and (5, 16.5). The gM region is separated by the dashed line above, which satisfies the equation $M_{\rm G} = 1.8 \times (G_{\rm BP} - G_{\rm RP})_0 - 2.2$.

3.4.2. DGCM

In the M_Catalog_V1, there are 52,461 spectra classified as gM by LAMOST, among which there are cases of misclassification between dM and gM. To identify as many of the misclassified dM and gM samples as possible, we trained the CNN-dMgM model to classify all spectra in M_Catalog_V1 into dM and gM, with 52,225 spectra predicted as gM. The training data and labels are from M_Catalog_V1. In addition to removing spectra with an S/N_max below 5, as described in Section 3.4.1, we excluded spectra in the dM/gM region from Figure 6, where the classification results were inconsistent with those of LAMOST, to ensure the reliability of the training data and labels. From the filtered samples, we randomly selected 30,000 spectra for both dM and gM as the final training data, with the training and validation sets split in a 3:1 ratio. The confusion matrix for CNN-dMgM on the validation set is shown in Figure 8, with an average accuracy of 99.85%. In Figure 6, there are 36,202 spectra in the gM region. We combined the spectra classified as giants by LAMOST, the spectra classified as giants by the CNN-dMgM model, and the spectra in the giant star region of Figure 6, resulting in a total of 53,987 spectra as gM candidates. The remaining spectra were considered as dM. We manually classified the 53,987 spectra into dM and gM, using the distinguishing features (J. D. Kirkpatrick & D. W. J. McCarthy 1991; A. W. Mann et al. 2012; Y.-X. Guo et al. 2015) for dM and gM summarized in Table 3, and the results of the visual inspection are shown in Table 4. Among these, LAMOST misclassified 279 dM spectra as gM, 1799 gM spectra as dM, and some examples of the misclassified spectra by LAMOST are shown in Figure 9. During the manual inspection, we discovered 85 S-type stars, two F-type stars, and 1204 UNKNOWN spectra. The S-type star spectra are shown in Figure 7, and their identification standards follow the ZrO features mentioned in J. Chen et al. (2022). Neither the LAMOST 1D pipeline nor our CNN-SPT model classified S-type stars as a separate category, and they both lie in the gM region on the CMD, making it

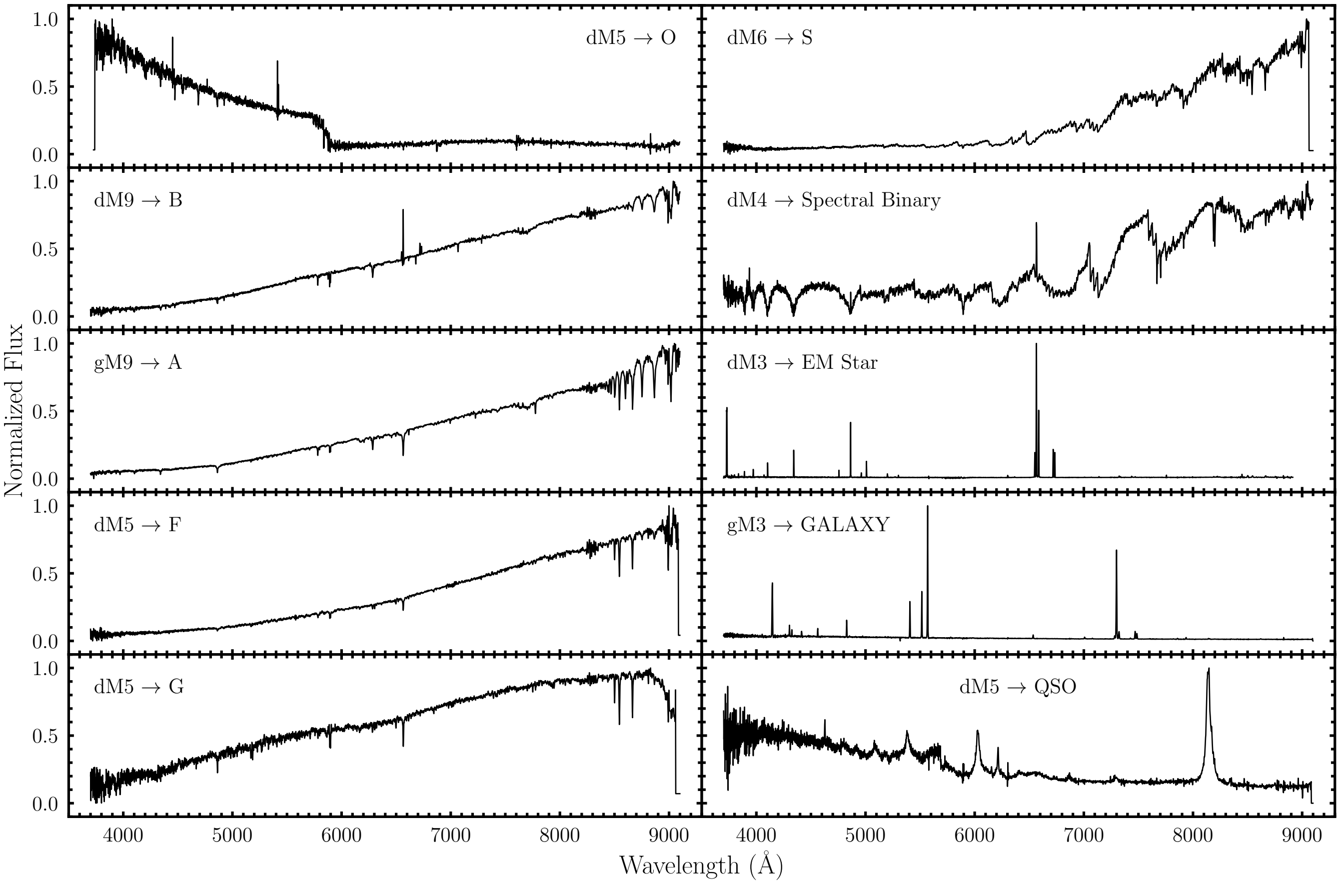

Figure 7. The examples of non-M-type spectra identified in this work. In all panels, the labels on the left and right of the arrows represent the spectral types published by LAMOST and the spectral types corrected in this work, respectively.

Table 1
The Visual Inspection Results of 13,436 Non-M-type Star Candidate Spectra

Spectral Type	B	A	F	G	M	Spectral Binary	Galaxy	QSO	Unknown
Number	1	3	1	5	9530	484	73	18	3321

Table 2
The Visual Inspection Results of 16,880 Non-M-type Spectra in the LAMOST DR8 M-type Star Catalog

Spectral Type	O	B	A	F	G	Spectral Binary	EM Star	Galaxy	QSO	Unknown
Number	1	115	14	49	16	45	54	45	46	16,495

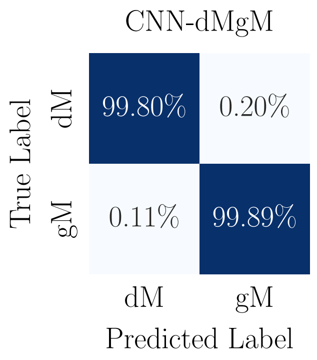

Figure 8. Confusion matrix of the CNN-dMgM model on the validation set.

understandable that these S-type stars were found during the manual check. For the spectra directly labeled as dM, we randomly inspected about 50,000 spectra to test if any gM spectra were mixed into the dM samples. The results show that, except for 419 UNKNOWN spectra, the rest were all dM. In the previous manual check of gM and dM spectra, a total of 1710 spectra were reclassified as non-M-type (mostly UNKNOWN), and were stored in the non-M_Catalog_V2. The remaining 870,518 spectra of M-type stars were stored in the M_Catalog_V2. With the removal of non-M spectra completed, the non-M_Catalog_V1 and non-M_Catalog_V2 were combined into non-M_Catalog, comprising 5,616 spectra in total.

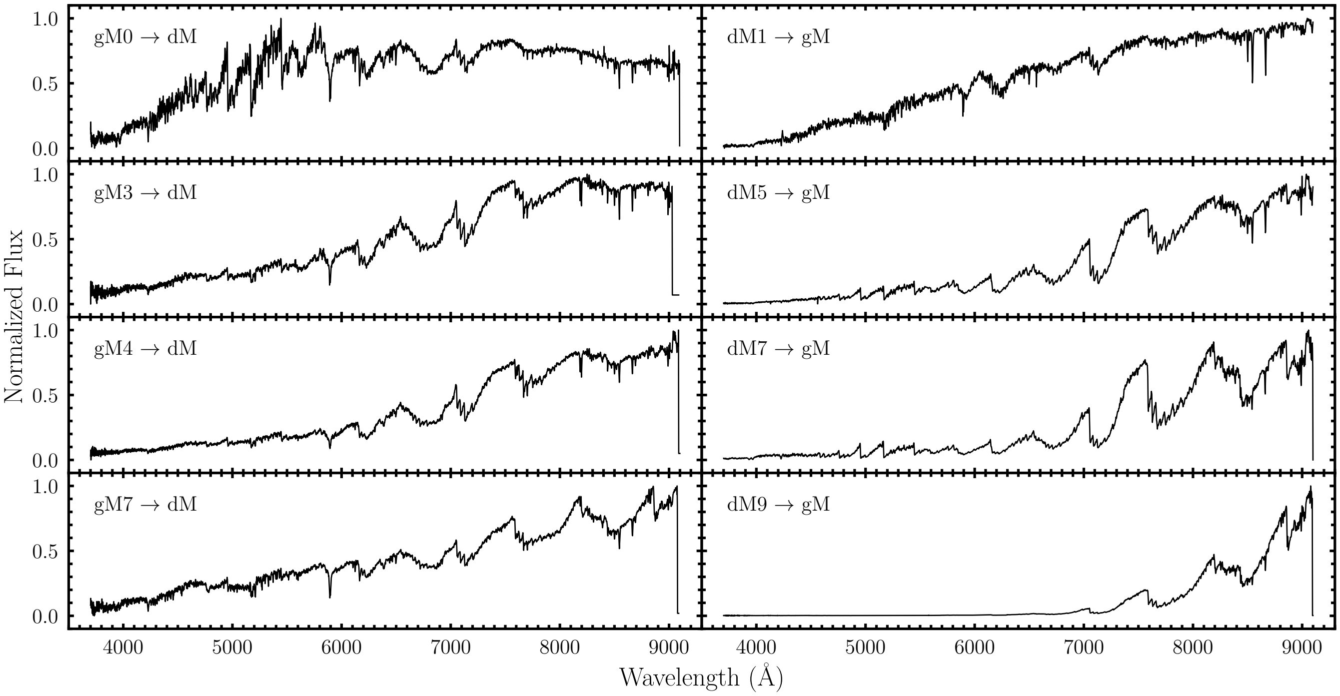

Figure 9. Examples of spectra with incorrect dM/gM classification from LAMOST. In all panels, the labels on the left and right of the arrows represent the luminosity classes published by LAMOST and the luminosity classes corrected in this work, respectively.

Table 3
Criteria[a] for Manually Classifying dMs and gMs

Feature	CaH	K I Doublet	Na I Doublet	Ca II Triplet
λ[b] (Å)	6946−7050	7665, 7699	8183, 8195	8498, 8542, 8662
dM	Dip	Deep	Deep	Shallow
gM	Flat	Shallow	Shallow	Deep

Notes.

[a] The classification criteria for dM and gM were summarized from J. D. Kirkpatrick & D. W. J. McCarthy (1991), A. W. Mann et al. (2012), and Y.-X. Guo et al. (2015).

[b] The air wavelengths of the features are from Table 5 in J. D. Kirkpatrick & D. W. J. McCarthy (1991). Since the LAMOST spectra are in vacuum wavelengths, for consistency, we converted the air wavelengths of the features to vacuum wavelengths during the manual inspection of the spectra.

3.4.3. RVMM

In order to correct the LAMOST RV measurement errors as much as possible, we measured the RVs of spectra in M_Catalog_V2 using the TM method and the Doppler shift of absorption lines (DSAL) method. By comparing these measurements with LAMOST RVs, we identified spectra where the LAMOST RVs might be erroneous, and we corrected the RVs through manual inspection. The specific procedure of the TM method is as follows:

1. Determining the best template (see Section 2.4 for a detailed description of the templates) and initial RV value. Assume that the observed spectrum's RV $\in \{60n | -10 \leqslant n \leqslant 10, n \in \mathbb{Z}\}$ (km s^{-1}), and calculate the χ^2 value between a single template spectrum and the observed spectrum:

$$\chi^2(\mathrm{RV}) = \frac{1}{N}\sum_{i=1}^{N} |O(\mathrm{RV}, \lambda_i) - P_k(\lambda_i) \times S(\lambda_i)|^2. \quad (2)$$

Table 4
The Results of the Manual Inspection of 53,987 gM Candidate Spectra

Spectral type	dM	gM	F	S	Unknown
Number	2671	50,025	2	85	1204

Here, N is the number of wavelength points, λ_i is the ith wavelength value, O is the flux of the observed spectrum, S is the flux of the template spectrum, and $P_k(\lambda)$ is the kth order polynomial used to reduce the errors caused by the inaccuracies in the continuum of the observed spectrum. Referring to Section 3.3 of S. Zhang et al. (2021), we set $k = 4$, and the polynomial coefficients of $P_k(\lambda)$ can be obtained by minimizing Equation (2). Then, we fitted the Gaussian profile to the χ^2 (RV) curve to determine the line center and the minimum point, which provides the RV value and the corresponding χ^2 value for the single template. We identified the template with the smallest χ^2 as the best template, and the RV derived from this template was taken as the initial RV value.

2. Calculating the final RV and error. After subtracting the initial RV value, we applied a velocity shift RV $\in \{n | -500 \leqslant n \leqslant 500, n \in \mathbb{Z}\}$ (km s^{-1}) to the observed spectrum, and used the best template to measure the RV again according to step 1. The residuals between the new RV measurement and the applied shift were then calculated. The final RV was determined as the initial RV plus the mean of the residuals, and the RV error was the standard deviation of the residuals.

This work employed two variations of the DSAL method, using eight absorption lines as shown in Table 5. The first method (DSAL I) strictly followed the procedure outlined in Section 3.2 of S. Zhang et al. (2019). Since this method

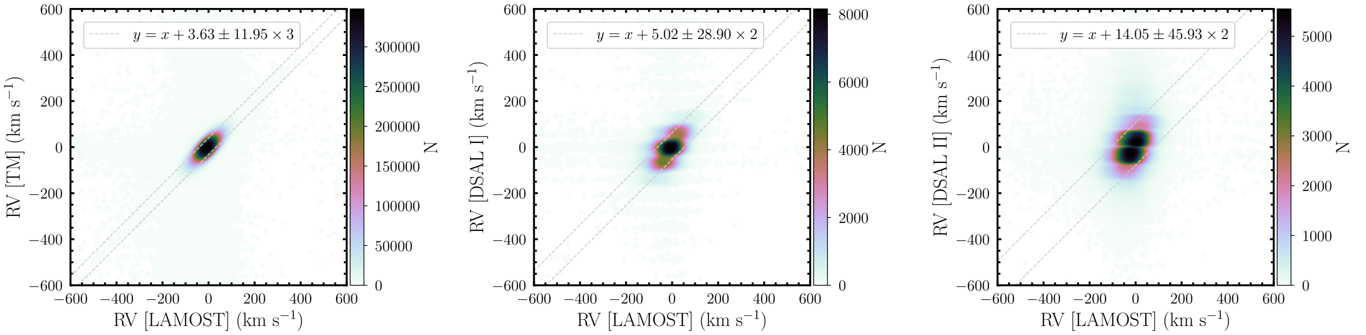

Figure 10. Comparison scatter plot of RVs derived from the TM method and the two methods based on measuring the Doppler shift of absorption lines (DSAL I/DSAL II) with LAMOST RVs. In the left panel, the points within the dashed line represent those removed iteratively after a 3σ cut, while in the middle and right panels, the points within the dashed lines correspond to those removed iteratively after a 2σ cut. The expression for the dashed lines is provided in the upper left corner of each panel, where 3.63, 5.02, and 14.05 are the means of RV residuals, and 11.95, 28.90, and 45.93 are the standard deviations of RV residuals. The number of points outside the dashed line in the left panel corresponds to the total number of points in the middle and right panels. In the middle and right panels, the number of points outside the dashed line are 13,076 and 18,436, respectively. Together with the spectra with LAMOST RVs having absolute values greater than 150 km s^{-1}, a total of 34,961 spectra require manual inspection to determine the RV.

Table 5
The Absorption Lines Used in the DSAL[a] Method

Absorption line	K I	K I	Na I	Na I	Ti I	Ca II	Ca II	Ca II
λ (Å)	7667.0089	7701.0825	8185.5054	8197.0766	8437.2600	8500.3600	8544.4400	8664.5200

Note.
[a] The RV was calculated by measuring the Doppler shift of the absorption lines. Two DSAL methods were used in this study: DSAL I, as described in S. Zhang et al. (2019), and DSAL II, which includes some adjustments based on DSAL I.

requires at least three absorption lines with consistent Doppler shifts for an accurate RV measurement (the mean and standard deviation of the RVs obtained from these absorption lines serve as the final RV and error), we designed a second method (DSAL II) to address cases where DSAL I cannot provide a result. DSAL II iteratively removed RV values that lie outside 1σ from the measurements of the eight absorption lines. If, after n iterations, the remaining RVs have a standard deviation less than 20 km s^{-1} and more than one RV value, the iteration is terminated, and the mean and standard deviation of the remaining RVs are taken as the final RV and error. If fewer than two RVs remain after the nth iteration, the mean and standard deviation from the $(n - 1)$th iteration are used instead. DSAL II ensures a measurement even for spectra that DSAL I cannot handle, though the precision may be lower for low-quality spectra.

Next, we outline the process of selecting spectra with potentially erroneous LAMOST RVs. First, we compare the LAMOST RVs with the results from the TM method. If they are consistent within 3σ (the region between the two dashed lines in the left panel of Figure 10), we consider the LAMOST RV reliable. If not, we compare the LAMOST RVs with the results from the DSAL method (using DSAL I if available, otherwise using DSAL II). If the LAMOST and DSAL RV measurements are consistent within 2σ (the region between the two dashed lines in the middle and right panels of Figure 10), the LAMOST RV is considered reliable; otherwise, we manually inspect the spectra to determine the RV. Second, for spectra with reliable LAMOST RVs, we also manually verify those with absolute RV values greater than 150 km s^{-1} to ensure the RVs are accurate.

As shown in Figure 10, from left to right, the panels compare the RVs measured using the TM method, DSAL I method, and DSAL II method with the LAMOST RVs. In each panel, points inside the dashed lines indicate consistent RVs, while points outside the dashed lines indicate discrepancies. Ultimately, we identified 31,512 spectra from LAMOST with potentially erroneous RV measurements (corresponding to the 13,076 and 18,436 points outside the dashed lines in the middle and right panels of Figure 10). Among the spectra for which we considered the LAMOST RV reliable, there were 3449 spectra with RV absolute values greater than 150 km s^{-1}. The total number of spectra requiring manual inspection, combining both groups, is 34,961. For these spectra, we moved the theoretical wavelengths of the eight absorption lines in Table 5 according to the LAMOST, TM, DSAL I, and DSAL II RV measurements and marked them for further inspection, selecting a more accurate RV as the final value. During the manual inspection, two categories of spectra had unreliable RVs for all four methods. We adjusted the TM and DSAL methods and remeasured the RVs for these spectra: (1) For spectra with red-end anomalies, we remeasured their RVs using the TM method with wavelength limited to the left of 7500 Å (TML7500). (2) For spectra with emission lines, we remeasured their RVs using the Doppler shift of emission lines (DSEL) method, which is analogous to DSAL II, and the eight emission lines used are listed in Table 6. There were also two categories of spectra for which reliable RVs could not be determined. For these, we set the RV to null. These two categories are (1) spectra with insufficient quality to determine an accurate RV and (2) spectra with wavelength calibration errors during LAMOST spectral data processing caused abnormal absorption line positions. The RV inspection results for the 34,961 spectra are summarized in Table 7, and the corrected RVs were stored in M_Catalog_V3. Columns (2)–(7) of Table 7 show the sources and quantities of manually inspected RVs, among which columns (3)–(7) correspond to the updated RVs, totaling 12,900. The last two columns show

Table 6
The Emission Lines Used in the DSEL[a] Method

Emission Line	N II	Hα	N II	S II	S II	Ca II	Ca II	Ca II
λ (Å)	6549.8600	6564.6000	6585.2700	6718.2940	6732.6730	8500.3600	8544.4400	8664.5200

Note.
[a] The RV was calculated by measuring the Doppler shift of the emission lines.

Table 7
The Results of the Manual Inspection of the RV for 34,961 Spectra

rv_from[a] (1)	LAMOST (2)	TM[b] (3)	DSAL I[c] (4)	DSAL II[d] (5)	TML7500[e] (6)	DSEL[f] (7)	NoRV_lowQuality[g] (8)	NoRV_waveErr[h] (9)
Number	21,972	8278	995	3543	35	49	76	13

Notes.
[a] The source of the RV, consistent with the field names in the recommended catalog (i.e., Table 9).
[b] TM method.
[c] The first DSAL method.
[d] The second DSAL method.
[e] TM method with wavelength lower than 7500 Å.
[f] The DSEL method mentioned in Table 6.
[g] RV could not be determined due to the low quality of the spectrum.
[h] RV could not be determined due to an error in the spectral wavelength calibration.

the number of spectra for which reliable RVs could not be provided due to the two specific issues, totaling 89.

It should be noted that, for spectra without manual inspection, we adopted the LAMOST RV as the final value. Among these spectra, 3.56% show that the LAMOST RV is consistent with TM but not with DSAL, whereas 7.59% show that the LAMOST RV is consistent with DSAL but not with TM. These two cases highlight potential risks in our RV determinations: (1) the LAMOST and TM RVs are consistent with each other but may nevertheless deviate from the true value; (2) the same issue may arise for the LAMOST and DSAL RVs. Even under the most unfavorable assumption, however, only about 11% of the RV results would exhibit relatively large errors.

Figure 11 shows examples of spectra with corrected RVs. Panels 1–3 display the spectra with normal, red-end anomaly, and emission-line features. The red-end anomaly occurs when incandescent lamps are inadvertently left on during observations, contaminating the spectra with spurious features.[11] Panels 4 and 5 display spectra for which accurate RVs could not be determined, corresponding to low-quality spectra and those with wavelength calibration errors. The gray and green dashed vertical lines represent the wavelengths of absorption or emission lines shifted according to the LAMOST RV or the corrected RV, respectively, and the RV values are annotated in the top left corner. As shown in panels 1–3, the corrected RVs are more reliable than the original LAMOST RVs. Notably, in panel 5, the RV of $-1238.81\,\mathrm{km\,s^{-1}}$ measured by LAMOST appears reasonable based on the Doppler shift of the absorption lines. However, for stars, a line-of-sight velocity greater than $1000\,\mathrm{km\,s^{-1}}$ is unusually high, and we need to confirm whether they are hypervelocity stars or if there is an issue with spectral processing. After inspection by LAMOST official personnel, a wavelength calibration error was confirmed in this spectrum.

3.4.4. SPMM

In this work, we used the "label transfer + parameter prediction" strategy for measuring parameters of M-type stars. In this work, "label transfer" refers to the approach of using LAMOST low-resolution M-type stellar spectra and high-precision M-type stellar parameters measured from APOGEE high-resolution spectra to train deep learning models. After the model learns the relationship between low-resolution spectral features and stellar parameters, this knowledge will be subsequently "transferred" to other LAMOST low-resolution M-type stellar spectra, enabling more reliable stellar parameter measurements. Compared to directly applying models trained on synthetic spectra to observed spectra for stellar parameter prediction, the "label transfer" approach significantly reduces systematic errors arising from the "synthetic gap" (V. M. Passegger et al. 2020), which is particularly advantageous given that current atmospheric models for M-type stars remain relatively immature, with significant discrepancies between theoretical and observed spectra (H. R. A. Jones et al. 2023). Furthermore, the "parameter prediction" methodology—directly estimating stellar parameters from spectra—generally has higher efficiency compared to "parameter inference" approaches.

We used the CNN-TLMA model (the network architecture is shown in Figure 2) to measure four stellar parameters (T_{eff}, $\log g$, [M/H], and [α/M]) for all spectra in M_Catalog_V3 and provided the associated errors. The measurement results were subsequently compiled into the recommended catalog. It is important to note that, as described in Section 3.2, the input

---

[11] After completing the entire workflow (see Figure 1), we compiled statistics for the 35 red-end-anomalous spectra, all of which were visually confirmed to be dMs. Our statistic results are as follows: CNN-SPT and CNN-WDM classified 19 and 18 spectra as M, respectively; for those spectra that at least one of these two models labeled as non-M, visual inspection confirmed them to be M-type stars; CNN-dMgM classified 26 spectra as dM, and the remaining nine spectra were confirmed as dMs by visual inspection; and for CNN-TLMA, only three spectra had predicted parameters that passed the quality assessment cuts and were recommended for use. Given the extensive red-end anomalies in these spectra, relatively lower classification and parameter prediction accuracies for this subset are to be expected.

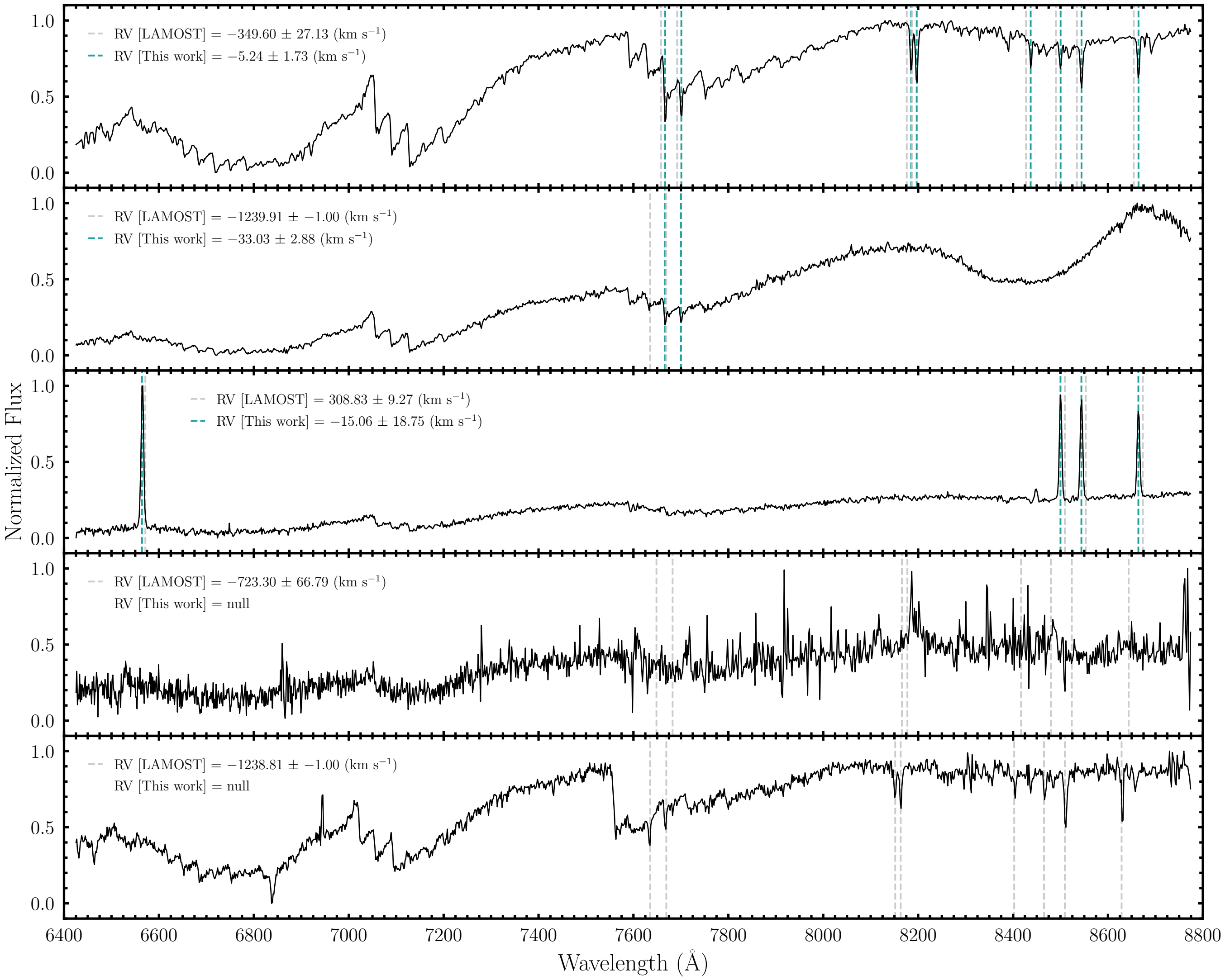

Figure 11. Examples of spectra with incorrect RV measurements from LAMOST. The LAMOST RV and those corrected in this work are given in all panels. The top three panels show normal spectra, red-end abnormal spectra, and spectra with emission lines where the LAMOST RV is incorrectly measured. The bottom two panels show spectral examples with incorrect RV measurements of LAMOST, for which RV values cannot be provided in this work. These issues are due to poor spectral quality and wavelength calibration errors, respectively.

to CNN-TLMA is the spectrum shifted to the rest frame using the updated RVs from RVMM (see Section 3.4.3 for more details), and the RV shift is applied only for this module. The training data of the CNN-TLMA is from M_Catalog_V3, and the labels are the four stellar parameters provided by APOGEE DR16 (hereafter, unless otherwise specified, referred to as APOGEE). Beyond removing spectra with an S/N_max below 5, as described in Section 3.4.1, we further ensured that the `ASPCAP_CLASS`[12] was consistent with the DGCM (see Section 3.4.2 for more details) classification results to ensure the reliability of the training data and labels. All the filtered samples were used as the final training data, with 12,541 dM spectra and 3927 gM spectra. We trained 10 CNN-TLMA models for the dM and gM spectra using tenfold cross-validation, where the training data was randomly divided into 10 equal-sized subsets. In each fold, one subset was selected as the validation set, and the remaining nine subsets were used as the training set to train the model. The mean and standard deviation of the predictions from the 10 models were used as the final stellar parameters and their corresponding errors.

The residual statistics and loss values for these 20 models on their respective validation sets are summarized in Table 8. It can be seen that the performance differences on the validation set across the folds are minimal, so we only show the comparison of the four stellar parameters predicted by the model with the minimum validation loss in Figure 12. It can be seen that there is a good consistency between the predicted values and the true labels, with outliers mostly being low S/N spectra. The mean predictions from multiple models smooth out the bias of individual models, improving the robustness of the predictions, while the standard deviation effectively quantifies the uncertainty between models, providing confidence in the results. Furthermore, the tenfold cross-validation fully utilizes the data, mitigates the risk of overfitting, and enhances the model's generalization ability and the reliability of the results. Therefore, it is reasonable to use a model ensemble, taking the mean of the predictions from the 10 models as the final result, with the standard deviation as the

---

[12] The `ASPCAP_CLASS` is a field provided in the APOGEE DR16 parameter catalog, representing the temperature class of the best-fitting spectrum.

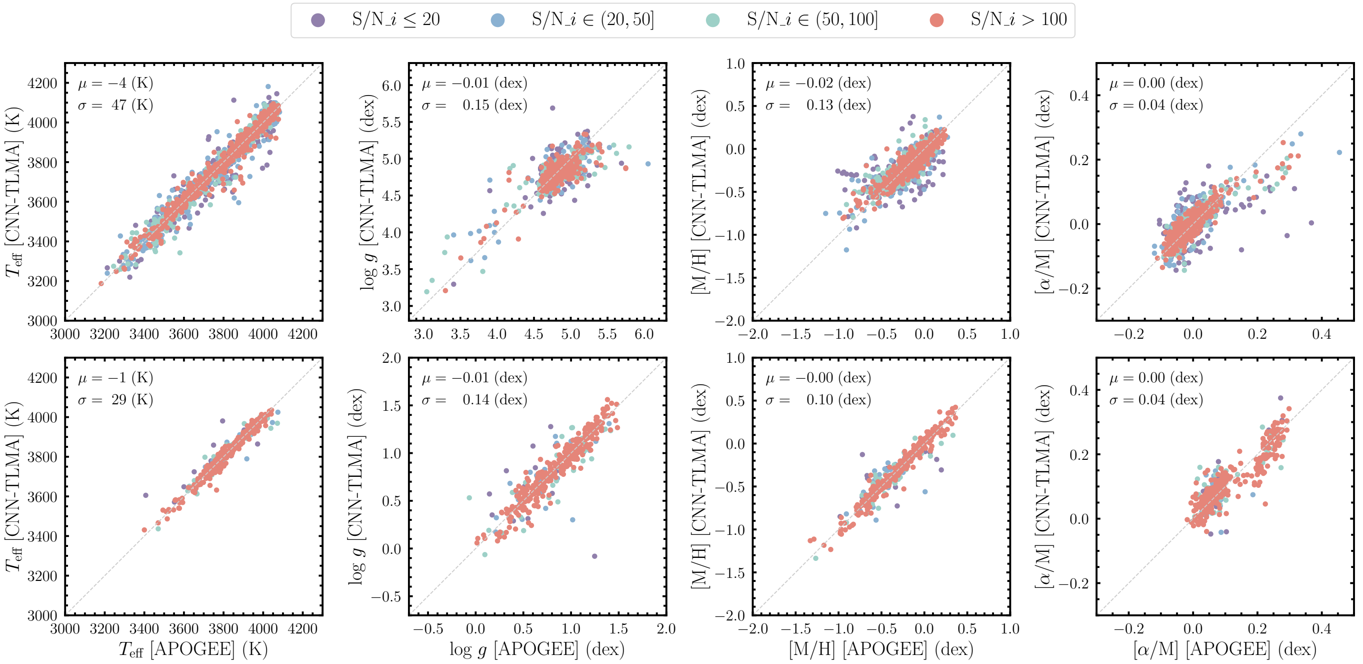

Figure 12. Comparison of the CNN-TLMA model predictions (with the smallest validation loss in tenfold cross-validation) and APOGEE data. The first row presents results for dM, while the second row shows results for gM. Spectra in different S/N ranges are represented by scatter points in distinct colors.

Table 8
Residual Statistics and Loss Values for the CNN-TLMA Models of dM and gM Stars on the Validation Set in Tenfold Cross-validation

Model ID	$\Delta T_{\rm eff}$ (K)	Δ log g (dex)	Δ [M/H] (dex)	Δ [α/M] (dex)	Validation Loss
dM					
0	3 ± 50	−0.00 ± 0.15	−0.01 ± 0.13	0.00 ± 0.04	0.282
1	3 ± 51	0.04 ± 0.16	0.01 ± 0.14	−0.00 ± 0.04	0.323
2	−17 ± 52	−0.01 ± 0.17	−0.01 ± 0.14	0.00 ± 0.04	0.322
3	−4 ± 47	−0.01 ± 0.15	−0.02 ± 0.13	0.00 ± 0.04	0.278
4	−3 ± 51	0.02 ± 0.16	0.00 ± 0.13	−0.00 ± 0.04	0.300
5	7 ± 52	0.00 ± 0.16	−0.00 ± 0.14	−0.00 ± 0.04	0.304
6	−5 ± 51	0.02 ± 0.17	0.01 ± 0.13	0.01 ± 0.04	0.295
7	3 ± 54	0.01 ± 0.16	0.03 ± 0.14	0.01 ± 0.04	0.302
8	5 ± 55	−0.02 ± 0.17	0.02 ± 0.15	−0.00 ± 0.05	0.364
9	6 ± 52	0.00 ± 0.16	0.03 ± 0.13	−0.00 ± 0.04	0.283
gM					
0	−1 ± 37	−0.01 ± 0.18	−0.00 ± 0.10	−0.00 ± 0.04	0.185
1	−1 ± 29	−0.01 ± 0.14	−0.00 ± 0.10	0.00 ± 0.04	0.137
2	9 ± 30	−0.00 ± 0.14	−0.01 ± 0.11	0.00 ± 0.05	0.161
3	−7 ± 32	−0.03 ± 0.14	0.00 ± 0.09	0.00 ± 0.04	0.153
4	3 ± 40	0.00 ± 0.16	−0.02 ± 0.11	0.00 ± 0.05	0.212
5	1 ± 28	0.00 ± 0.13	0.01 ± 0.10	0.01 ± 0.05	0.159
6	−1 ± 33	0.01 ± 0.15	0.01 ± 0.10	0.00 ± 0.04	0.146
7	−5 ± 35	0.03 ± 0.14	0.01 ± 0.10	0.00 ± 0.04	0.160
8	−0 ± 29	0.01 ± 0.15	0.01 ± 0.12	−0.00 ± 0.04	0.168
9	9 ± 37	0.00 ± 0.21	−0.00 ± 0.11	0.01 ± 0.04	0.205

error quantification metric. For the training data, the integrated predicted results (including $T_{\rm eff}$, log g, [M/H], and [α/M]) show the systematics and dispersions relative to APOGEE as follows: (1) for dM stars 0 ± 52 K, 0.00 ± 0.16 dex, 0.01 ± 0.14 dex, and 0.00 ± 0.04 dex; (2) for gM stars 1 ± 34 K, 0.00 ± 0.16 dex, 0.00 ± 0.10 dex, and 0.00 ± 0.04 dex.

4. Result

4.1. Quality Assessment Cuts and Recommended Catalog

As mentioned earlier, RVMM (described in detail in Section 3.4.3) corrected the erroneous RVs from LAMOST. SPMM (described in detail in Section 3.4.4) estimated the stellar parameters and their errors ($T_{\rm eff}$, log g, [M/H],

Table 9
Recommended Catalog

Field	Unit	Description
obsid	⋯	The unique spectral ID from LAMOST DR10.
ra	deg	Right ascension from LAMOST DR10.
dec	deg	Decl. from LAMOST DR10.
snr_u/g/r/i/z	⋯	The signal-to-noise ratio in the *u*, *g*, *r*, *i*, or *z* band.
orp_u/g/r/i/z	⋯	The proportion of ormask values that are nonzero in the *u*, *g*, *r*, *i*, or *z* band.
subclass	⋯	The stellar spectral type from LAMOST DR10.
luminosity_class	⋯	The corrected dM/gM classification result.
rv	km s^{-1}	The corrected RV.
rv_err	km s^{-1}	The error in RV.
rv_from	⋯	The source of RV.
teff	K	Effective temperature.
teff_err	K	The error of the effective temperature.
logg	dex	Surface gravity.
logg_err	dex	The error of the surface gravity.
m_h	dex	Metallicity.
m_h_err	dex	The error in the metallicity.
alpha_m	dex	Alpha element abundance.
alpha_m_err	dex	The error of the alpha element abundance.
rv_flag[a]	⋯	The RV validity flag.
parameter_flag[b]	⋯	The stellar parameter quality flag.
source_id	⋯	The unique source identifier from Gaia DR3.
r_med_geo	pc	The median of the geometric distance posterior from C. A. L. Bailer-Jones et al. (2021).
ebv[c]	mag	The color excess $E(B - V)$.
bp_rp_0[d]	mag	The extinction-corrected Gaia $G_{\rm BP} - G_{\rm RP}$ color.
M_G_0	mag	The absolute magnitude $M_{\rm G}$ in Gaia's *G* band, calculated using Equation (1).
CMD_flag[e]	⋯	The Gaia astrometric parameter quality flag.
CMD_pos[f]	⋯	The position of sources with CMD_flag=1 on the Gaia CMD.
W1_W2_0[g]	mag	The extinction-corrected AllWISE (R. M. Cutri et al. 2021)W1 − W2 color.
e_W1/W2	mag	The mean error of AllWISE W1/W2 magnitude.

Notes. A machine-readable version of this table is available online and at doi:10.12149/101668.

[a] rv_flag = 1 indicates RV is recommended for use, 0 indicates RV is unavailable or there may be wavelength calibration issues in the spectrum.

[b] parameter_flag = 1 indicates that the stellar parameters are recommended for use, while 0 indicates they are not recommended for use.

[c] $E(B - V)$ is determined from the 3D dust map Bayestar19 (G. M. Green et al. 2019) using r_med_geo.

[d] The extinction coefficient is from L. Casagrande & D. A. VandenBerg (2018).

[e] Based on the five equations in Section 3.4.1, the Gaia astrometric data are quality-filtered. CMD_flag = 1 indicates that the Gaia astrometric data are reliable, while 0 indicates they are unreliable.

[f] CMD_pos = "dM" indicates the star is in the dM region of Figure 6, "gM" in the gM region, and "other" in the non-M region.

[g] The extinction coefficient is from R. Zhang & H. Yuan (2023).

(This table is available in its entirety in machine-readable form in the online article.)

and [α/M]) separately for dM and gM spectra. These parameters are included in the recommended catalog (a summary of the field descriptions is presented in Table 9) provided in this work, which also contains quality assessment cut flags for RV (`rv_flag`) and stellar parameters (`parameter_flag`). Further details on these flags are provided below.

1. Before 2012 January 14, some exposures in the LAMOST low-resolution survey were affected by issues with the wavelength calibration lamp in the red channel, which could have led to errors in RVs. To ensure data reliability, we applied a selection criterion to the `rv` values in the recommended catalog. The `rv_flag` is set to 1 if the following conditions are met (indicating that the RV is recommended for use); otherwise, it is set to 0 (indicating that the RV is either unavailable or not recommended for use).

   a. `rv` is not null.
   b. The spectrum was observed after 2012 January 14.

2. We applied quality assessment cuts to the four stellar parameters in the recommended catalog. For stellar parameters recommended for use, the `parameter_flag` is set to 1; otherwise, it is set to 0. Since the primary spectral features used in this work are concentrated around the *i* band, the accuracy of the predicted parameters is likely to be affected if the *i*-band spectrum has quality issues. Therefore, for spectra with S/N_*i* (S/N in the *i* band) less than or equal to 0, the `parameter_flag` is directly set to 0. For spectra with S/N_*i* greater than 0, the `parameter_flag` will be set through the following two steps:

   1. The errors of the stellar parameters are within a reasonable range.

      For spectra with the same S/N level, if the four stellar parameters predicted by SPMM are similar, their error levels should also be comparable. We divided the dM and gM samples into four groups based on S/N_*i*, corresponding to the following S/N_*i* ranges: (0, 20], (20, 50], (50, 100], and > 100. For samples in different S/N_*i* intervals, we used linear regression (LR) to fit the relationship between stellar parameter errors and both the stellar parameters and S/N_*i*. The specific formula is given below:

$$\hat{\sigma}_p = a_0 + a_1 \cdot {\rm S/N\_}i + a_2 \cdot T_{\rm eff} + a_3 \cdot \log g + a_4 \cdot [{\rm M/H}] + a_5 \cdot [\alpha/{\rm M}]. \tag{3}$$

      Here, $\hat{\sigma}_p$ represents the LR-predicted value of the stellar parameter error σ_p, where p corresponds to $T_{\rm eff}$, log g, [M/H], or [α/M]. We define the reasonable range of parameter errors as the region where the difference between the actual error and the LR-predicted error ($\sigma_p - \hat{\sigma}_p$) satisfies the following condition:

$$\sigma_p - \hat{\sigma}_p < {\rm mean}(\sigma_p - \hat{\sigma}_p) + 3 \cdot {\rm STD}(\sigma_p - \hat{\sigma}_p). \tag{4}$$

      Here, mean(·) represents the mean of $\sigma_p - \hat{\sigma}_p$, and STD (·) denotes its standard deviation. A smaller $\sigma_p - \hat{\sigma}_p$ is preferred, while excessively large values indicate reduced reliability of the stellar parameters. Therefore, the `parameter_flag` is initially set to 1 for stellar parameters that satisfy Equation (4), and to 0 otherwise.

Table 10
Recommended Range of Stellar Parameters

Stellar Parameter	dM	gM
$T_{\rm eff}$ (K)	[3225, 4125]	[3425, 4075]
log g (dex)	[4.35, 5.45]	[−0.05, 1.55]
[M/H] (dex)	[−0.85, 0.35]	[−1.35, 0.45]
[α/M] (dex)	[−0.13, 0.25]	[−0.03, 0.31]

2. The stellar parameters are within a reasonable range.
   We first identify reliable members with trustworthy stellar parameters from the training data used by SPMM based on the following criteria:
   a. `parameter_flag` = 1.
   b. `snr_u`, `snr_g`, `snr_r`, and `snr_z`> 0.
   c. `snr_i`> 20.
   d. `luminosity_class`, `ASPCAP_CLASS`, and `CMD_pos` agree on the dM/gM classification.

Here, `snr_u/g/r/i/z`, `luminosity_class`, and `CMD_pos` are fields provided in the recommended catalog (see Table 9). For the description of `ASPCAP_CLASS` refer to footnote 12 in Section 3.4.4. Based on this, the reasonable ranges of the four stellar parameters are obtained, as shown in Table 10. Subsequently, we apply the reasonable parameter ranges to the samples whose `parameter_flag` was initially set to 1, reassigning `parameter_flag` to 0 for those falling outside the ranges.

When using the RVs provided in the recommended catalog of this work, we suggest selecting those with `rv_flag`=1 (94% of the total spectra). For stellar parameters, we recommend using those with `parameter_flag`=1, corresponding to 716,207 dM spectra (87% of the total dM spectra) and 40,907 gM spectra (82% of the total gM spectra). Figure 13 displays the internal error levels of the recommended RVs and stellar parameters across different S/N_i intervals, where red corresponds to dM and blue corresponds to gM. As shown, the errors gradually decrease and tend to stabilize with increasing S/N_i. The average internal errors for dM/gM are, respectively, RV 6/3 km s^{-1}, $T_{\rm eff}$ 30/17 K, log g 0.07/0.07 dex, [M/H] 0.07/0.05 dex, and [α/M] 0.02/0.02 dex.

4.2. External Comparison

To facilitate subsequent analysis, before performing external comparisons, we define the following spectral quality criteria to ensure, to the greatest extent possible, the use of reliable parameters from both our work and the literature:

1. `snr_u` and `snr_g`> 0.
2. `snr_r`, `snr_i`, and `snr_z`> 20.
3. `orp_u`, `orp_g`, `orp_r`, `orp_i`, and `orp_z`< 1%.

Here, `orp_u/g/r/i/z` are fields provided in the recommended catalog (see Table 9).

4.2.1. RV

To assess the reliability of the RVs recommended in this work (corresponding to `rv_flag` = 1 in Table 9), we crossmatched with the RVs provided in Gaia DR3 (D. Katz et al. 2023). We only consider sources that meet the following criteria to maximize the use of reliable Gaia RVs:

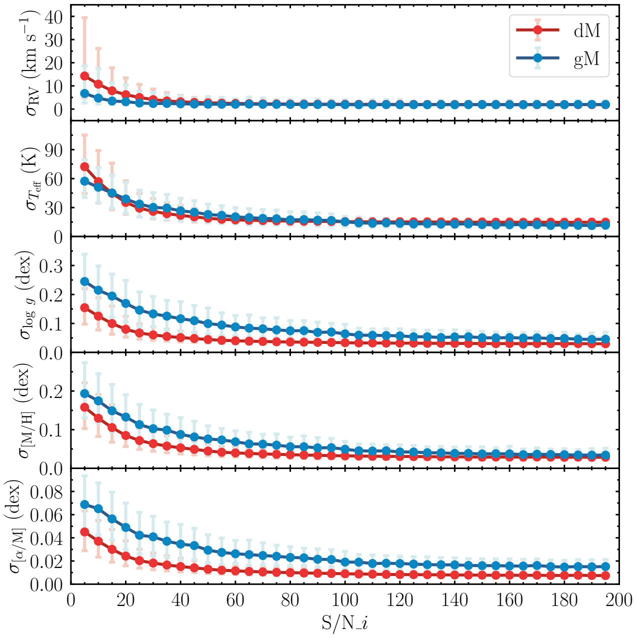

Figure 13. Errors of the recommended RVs and stellar parameters as a function of S/N_i. Each point represents the median value within the interval (S/N_i − 2.5, S/N_i + 2.5], and the error bars indicate the 16th and 84th percentiles in each bin. Spectra with S/N_$i \geqslant 200$ are not shown, as the associated errors remain nearly constant in this regime.

1. `radial_velocity_error` < 2 km s^{-1}.
2. `rv_expected_sig_to_noise` > 20.

Here, both of these fields are provided in the Gaia catalog. `radial_velocity_error` is the combined RV formal uncertainty, while `rv_expected_sig_to_noise` is the expected S/N in the combination of the spectra used to obtain the RV.

Figure 14 presents a comparison between the RVs provided in this work and those from Gaia. The upper panel shows high-quality spectra meeting the criteria defined in Section 4.2, while the lower panel shows low-quality spectra failing to satisfy the criteria. In the figure, the y-coordinates of blue points represent LAMOST RVs that were deemed reliable by RVMM (described in detail in Section 3.4.3), while gray plus signs (some of which extend beyond the plot boundaries and are not displayed) indicate LAMOST RVs that were deemed unreliable by RVMM, which were then updated by RVMM and shown as red points. As shown in Figure 14, for high-quality spectra (upper panel), the RVs recommended in this work are highly consistent with Gaia RVs, accurately correcting the measurement errors in the original LAMOST RVs. For low-quality spectra (lower panel), although the dispersion between the recommended RVs and Gaia RVs increases due to noise features sometimes being misidentified as absorption lines, a substantial improvement in accuracy over the original LAMOST RVs is still achieved.

4.2.2. Stellar Parameters

To assess the reliability of the stellar parameters recommended in this work (corresponding to `parameter_flag` = 1 in

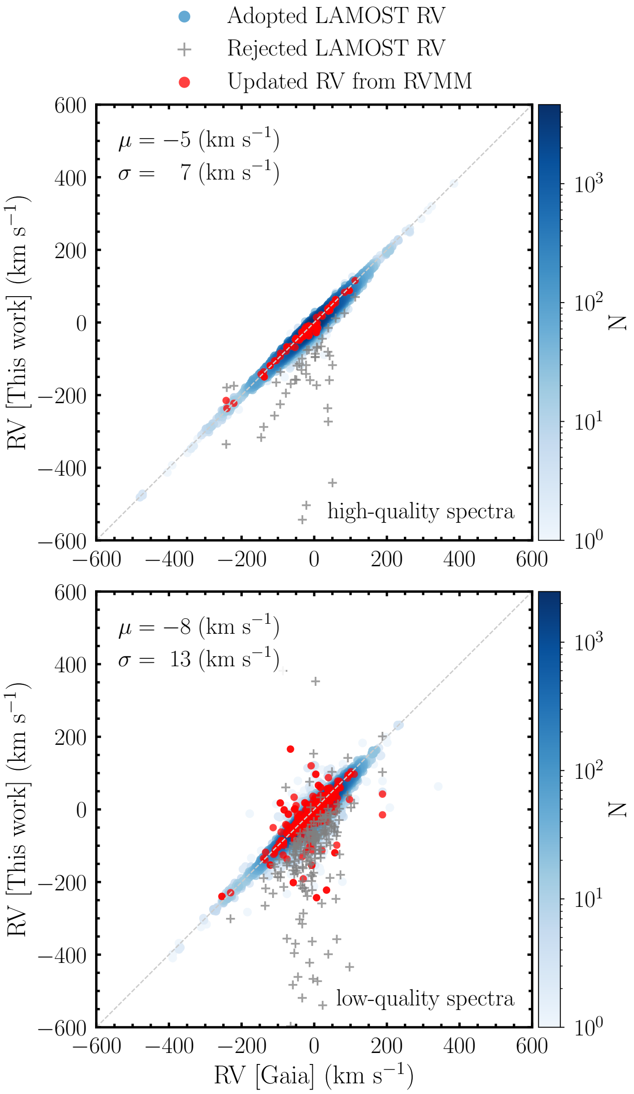

Figure 14. Comparison between the recommended RVs and the Gaia RVs. The upper and lower panels correspond to high-quality and low-quality spectra, respectively. The blue points and gray plus signs represent LAMOST RVs that were deemed reliable and unreliable by RVMM (described in detail in Section 3.4.3), respectively. The red points show the corresponding updated RVs from RVMM, with each red point paired with its corresponding gray plus sign. The μ and σ in each panel represent the systematic difference and dispersion between the recommended RVs and the Gaia RVs, respectively.

Table 9), we conducted comparisons not only with the parameters provided by the LASPM (B. Du et al. 2021), but also with those from J. Li et al. (2021, hereafter Li2021), M.-Y. Ding et al. (2022, hereafter Ding2022), D. Qiu et al. (2023, hereafter Qiu2023), and J. Liang et al. (2022, hereafter Liang2022).

LASPM used a TM algorithm and BT-Settl theoretical spectra to measure $T_{\rm eff}$, log g, and [M/H] for all M-type stars observed by LAMOST. Ding2022 employed the ULySS software package and template spectra generated with the MILES interpolator to determine $T_{\rm eff}$, log g, and [M/H] for a total of 763,136 spectra in LAMOST DR8. Li2021 applied the SLAM method, with stellar parameter labels from APOGEE DR16, to measure $T_{\rm eff}$ and [M/H] for 243,231 selected dM spectra in LAMOST DR6. Qiu2023, using the same SLAM method but with stellar parameter labels from APOGEE DR17, measured $T_{\rm eff}$, log g, [M/H], and [α/M] for 43,972 selected gM spectra in LAMOST DR9. Liang2022 adopted the principal component analysis + light gradient boosting machine method, utilizing stellar parameter labels from APOGEE DR16 and photometric data, to determine $T_{\rm eff}$, log g, and [M/H] for 37,979 stars.

Since none of the five studies provided quality flags for stellar parameters, and not all of them reported parameter errors, we uniformly applied the spectral quality criteria defined in Section 4.2, given that most studies derived stellar parameters from LAMOST spectra, to ensure the highest possible reliability of the parameters used in the comparison. Moreover, as different studies adopted varying methods to distinguish dM and gM stars, we aimed to minimize errors in stellar parameters caused by misclassification. To achieve this, when crossmatching with the five catalogs, we only included spectra for which the dM/gM classification was consistent across LAMOST, DGCM, and the Gaia CMD. Next, we will analyze the comparisons between the stellar parameters from this work and those provided by LASPM, Ding2022, Li2021, Qiu2023, and Liang2022 separately for dM and gM stars.

1. *LASPM*. Figures 15 and 16 display comparisons of $T_{\rm eff}$, log g, and [M/H] for dM and gM stars between LASPM and this work in the left column. The middle and right columns show comparisons between LASPM and APOGEE, and this work and APOGEE, respectively. For dM stars, the systematic differences and dispersions between LASPM and this work are −134 ± 77 K, 0.21 ± 0.23 dex, and −0.14 ± 0.32 dex for $T_{\rm eff}$, log g, and [M/H], respectively. For gM stars, the corresponding values are −204 ± 124 K, 2.03 ± 0.30 dex, and −0.61 ± 0.31 dex. As shown in Figures 15 and 16, the stellar parameters measured in this work generally show better consistency with APOGEE. There exist systematic structures between LASPM and this work, which are also present in the comparison between LASPM and APOGEE, suggesting that these structures likely originate from LASPM. Possible reasons for these structures include: (1) The synthetic spectra used in LASPM and APOGEE are generated from different atmosphere models: BT-Settl and MARCS, respectively. (2) A significant discrepancy between the theoretical spectra used in LASPM and the observed spectra. (3) The parameter grid of the theoretical spectra is relatively coarse, with no interpolation performed within the grid. (4) No iterative optimization was applied to further reduce the differences between the theoretical and observed spectra when determining stellar parameters. For the stellar parameters of gM stars, the measurements in this work are highly consistent with those from APOGEE, suggesting that the discrepancies between LASPM and this work are most likely caused by LASPM. For dM stars, we conduct a detailed analysis of the discrepancies in Figure 15. The red points indicate spectra for which the $T_{\rm eff}$ measured in this work is inconsistent with those from APOGEE. For these spectra, LASPM and APOGEE also show discrepancies in $T_{\rm eff}$, whereas LASPM and this work are highly consistent. This suggests that APOGEE may have incorrectly measured $T_{\rm eff}$ for these spectra. For most spectra, log g measurements from LASPM show significant discrepancies with this work, similar to those between LASPM and APOGEE, indicating that the

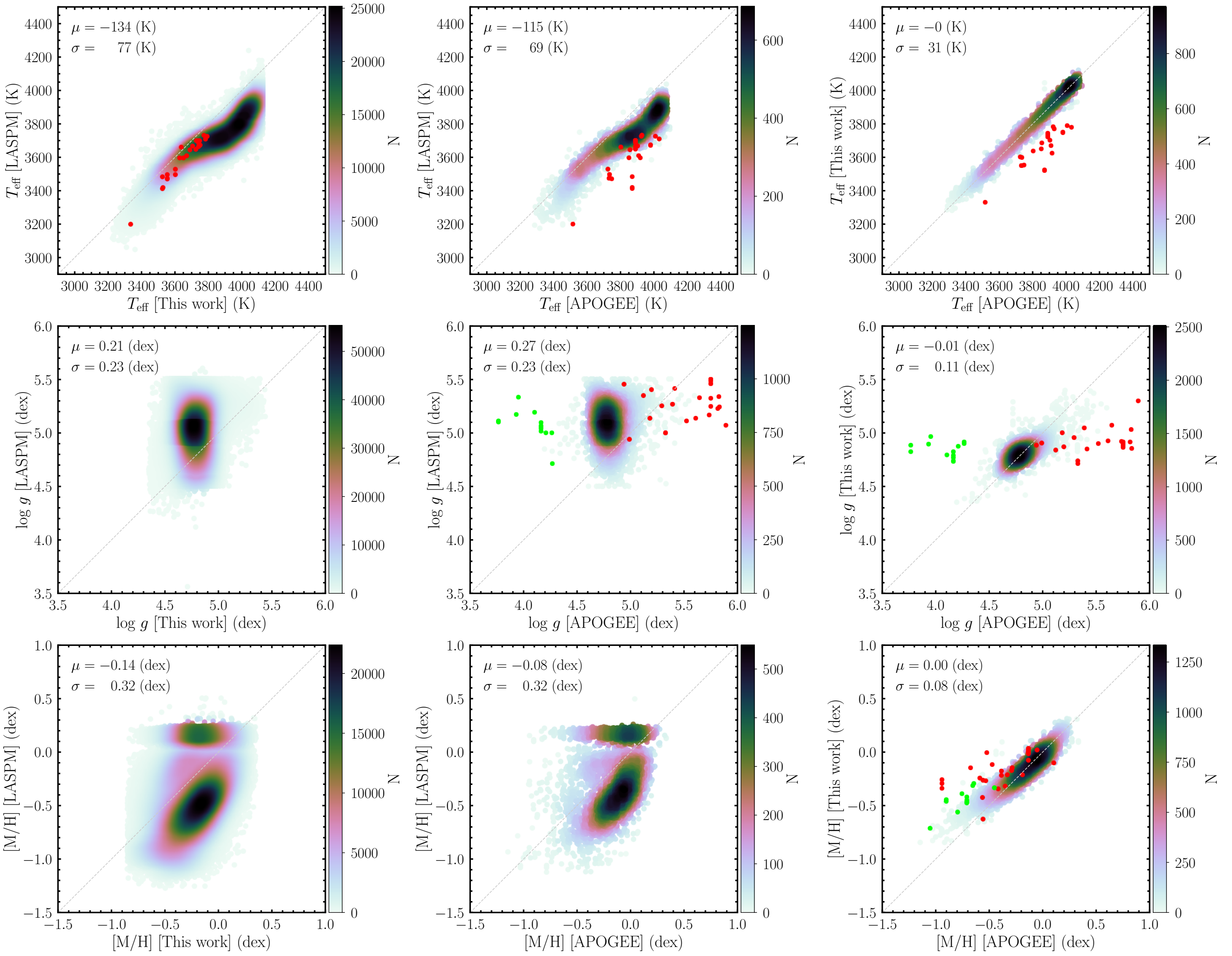

Figure 15. Comparison between the stellar parameters of dM stars derived in this work and those from LASPM (B. Du et al. 2021). The left, middle, and right columns show parameter comparisons between LASPM and this work, LASPM and APOGEE, and this work and APOGEE, respectively. From top to bottom, the parameters are $T_{\rm eff}$, log g, and [M/H]. Red dots indicate spectra for which the $T_{\rm eff}$ derived in this work and by APOGEE are inconsistent. Green dots indicate spectra with inconsistent log g between this work and APOGEE. The red or green dots in Figures 17, 19, 23, and 24 have the same meaning as in this figure and will not be explained again. A detailed analysis of these points is provided in Sections 4.2.2 and 4.3. The μ and σ in each panel represent the systematic difference and dispersion between the stellar parameters from different works, respectively.

measurements in this work are possible more reliable. The outliers where log g is overestimated in this work, compared to APOGEE, are marked with green points. For these green points, LASPM and APOGEE also show discrepancies in log g, suggesting that APOGEE may have incorrectly measured log g for these spectra. For the outliers where log g is underestimated in this work compared to APOGEE, we find that the vast majority correspond to the spectra (red points) for which APOGEE may have incorrectly measured $T_{\rm eff}$. This suggests that the log g measured by APOGEE for these spectra is also likely to be incorrect. Compared to APOGEE, the [M/H] provided in this work is systematically higher at the metal-poor end. This bias may result from the limited number of training samples in the metal-poor regime and potential labeling errors. It can be observed that most of the outliers with overestimated [M/H] at the metal-poor end correspond to the red and green points, which indicate spectra where APOGEE's parameter measurements may be problematic. In subsequent comparisons of stellar parameters with other studies, the causes of similar issues will not be discussed. Points and plus signs of the same color in later figures represent the same meanings.

2. *Ding2022*. Figures 17 and 18 display comparisons of $T_{\rm eff}$, log g, and [M/H] for dM and gM stars between Ding2022 and this work in the left column. The middle and right columns show comparisons between Ding2022 and APOGEE, and this work and APOGEE, respectively. For dM stars, the systematic differences and dispersions between Ding2022 and this work are -231 ± 58 K, 0.02 ± 0.10 dex, and -0.08 ± 0.17 dex for $T_{\rm eff}$, log g, and [M/H], respectively. For gM stars, the corresponding values are -149 ± 62 K, 0.39 ± 0.25 dex, and 0.16 ± 0.25 dex. Using the same analytical approach as in comparison 1, the systematic structures between Ding2022 and this work, for both dM and gM stars, are likely caused by Ding2022. For dM stars, the analysis of the red and green points is consistent with that in comparison 1. In

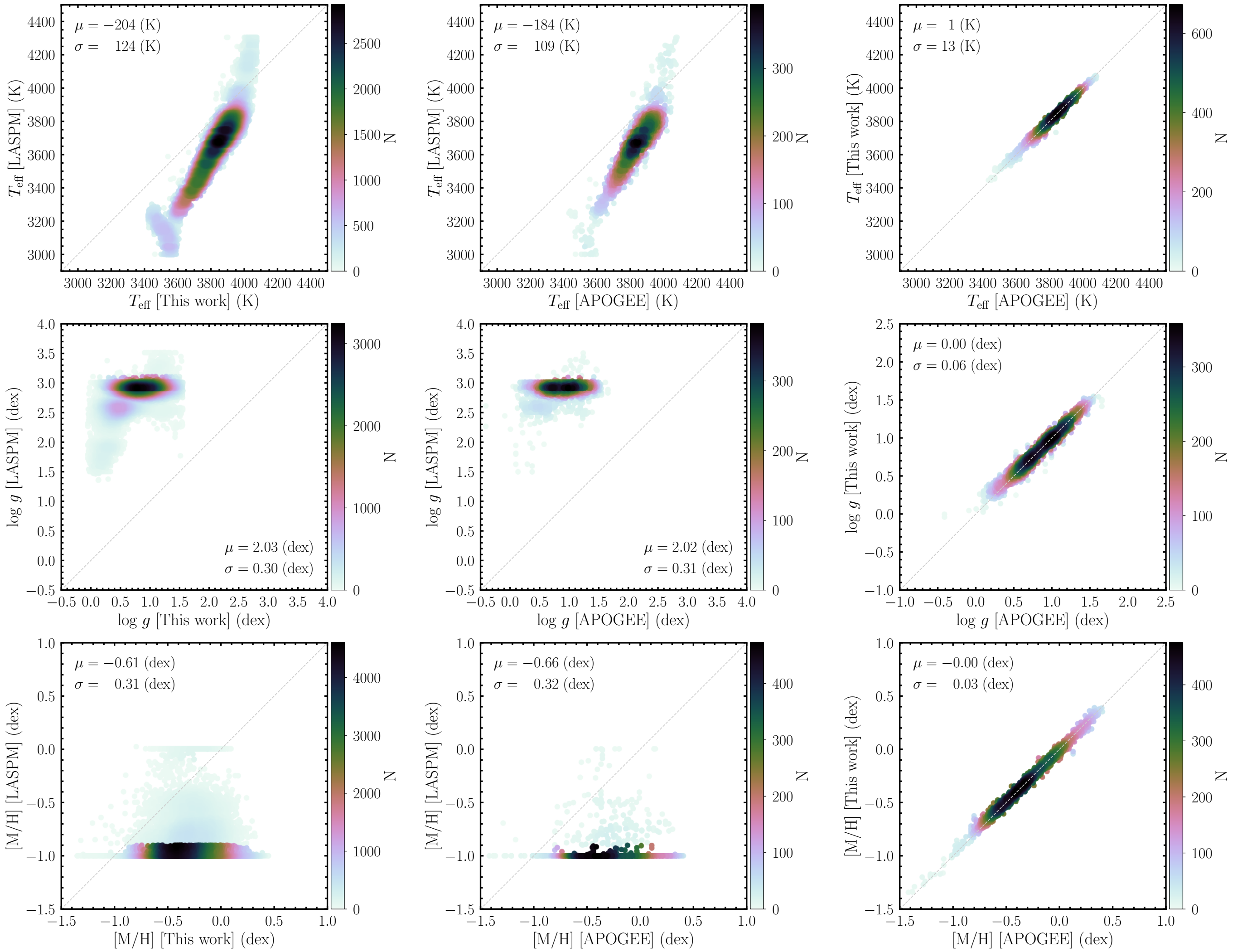

Figure 16. Comparison between the stellar parameters of gM stars derived in this work and those from LASPM. The left, middle, and right columns show comparisons between LASPM and this work, LASPM and APOGEE, and this work and APOGEE, respectively. From top to bottom, the parameters are $T_{\rm eff}$, log g, and [M/H]. The μ and σ in each panel represent the systematic difference and dispersion between the stellar parameters from different works, respectively.

the regions where log g derived by this work is below 4.55 dex or above 5.05 dex, the measurements in this work show noticeable discrepancies with Ding2022. The spectra in these two regions that have APOGEE parameters are marked with blue plus signs and blue points, respectively. When comparing with APOGEE, the log g values in this work exhibit larger dispersions but remain generally consistent, whereas the measurements from Ding2022 are mostly distributed in outlier positions, suggesting potential measurement issues in Ding2022. Additionally, Ding2022 includes a set of dM spectra with log g values below 4.35 dex, which fall outside the reliable log g range in this work. These spectra are marked with orange points. Since these spectra do not have APOGEE parameter crossmatches, they will be marked with the same color in the Kiel diagram (Figure 23) and analyzed accordingly. It is important to note that Ding2022 also contains another set of dM spectra with log g values below 3.5 dex, which exceed the limits of Figure 17; these spectra will be marked with orange plus signs in Figure 23. Both the orange points and orange plus signs will be analyzed in Section 4.3.

3. *Li2021*. Figure 19 displays comparisons of $T_{\rm eff}$ and [M/H] for dM stars between Li2021 and this work in the left column. The middle and right columns show comparisons between Li2021 and APOGEE, and this work and APOGEE, respectively. The systematic differences and dispersions between Li2021 and this work are 1 ± 51 K and −0.02 ± 0.18 dex for $T_{\rm eff}$ and [M/H], respectively. Overall, the $T_{\rm eff}$ and [M/H] from Li2021 and this work are consistent, as both adopted stellar parameter labels from APOGEE DR16. We find that compared to the $T_{\rm eff}$ measured in this work, the $T_{\rm eff}$ from Li2021 is systematically lower below 3600 K and systematically higher between 3600 K and 4000 K. The $T_{\rm eff}$ from Li2021 also exhibits some systematically lower outliers below 3600 K when compared to APOGEE; these spectra are marked with red plus signs. It can be observed that both the red points and red plus signs are located in the region where Li2021 and this work show discrepancies in $T_{\rm eff}$, whereas the red points lie in the region where Li2021 and APOGEE agree on $T_{\rm eff}$. Based on the analysis in comparison 1, the red points likely correspond to spectra for which APOGEE has an incorrectly measured $T_{\rm eff}$. We infer that the red plus signs may result from the SLAM-

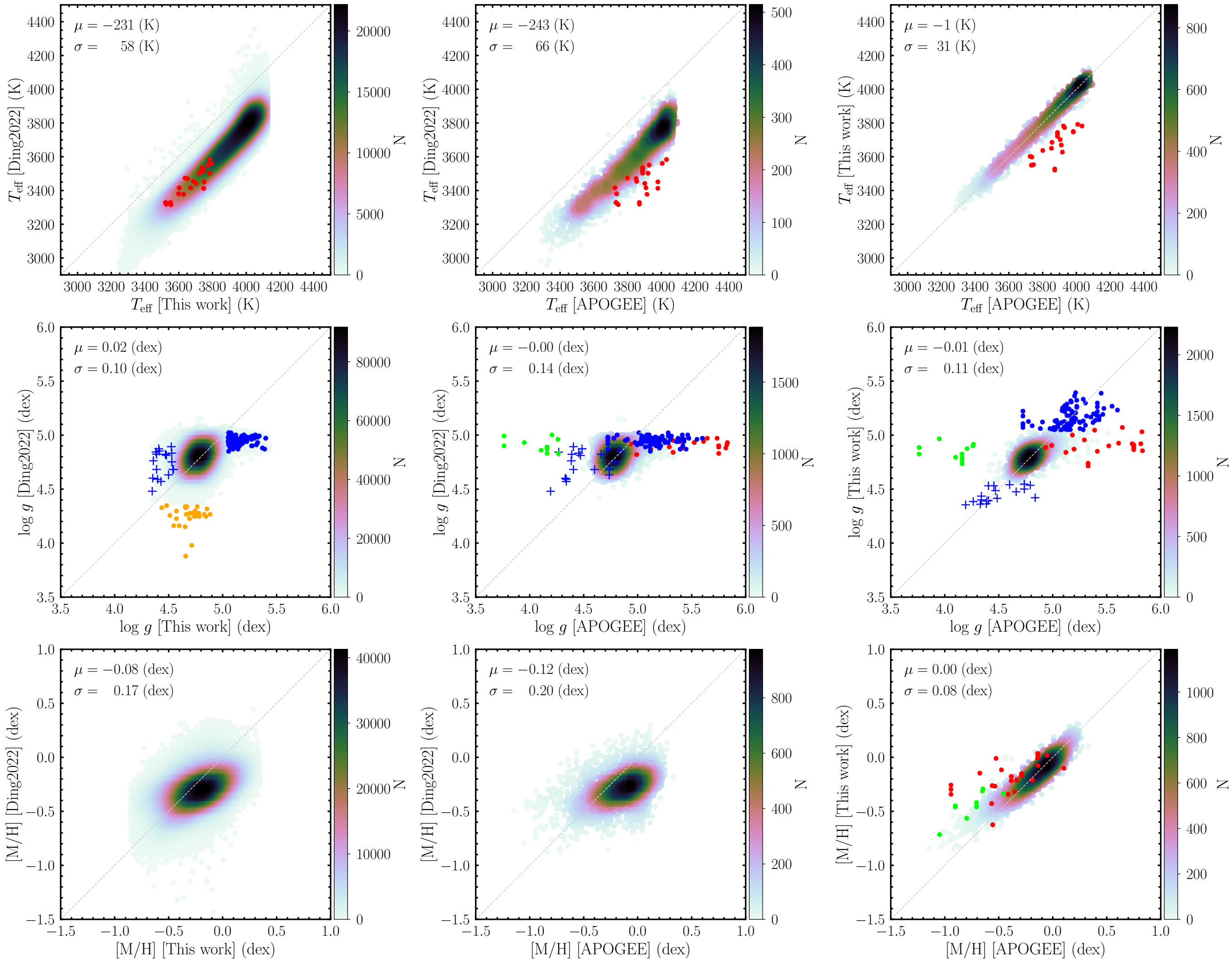

Figure 17. Comparison between the stellar parameters of dM stars derived in this work and those from Ding2022. The left, middle, and right columns show comparisons between Ding2022 and this work, Ding2022 and APOGEE, and this work and APOGEE, respectively. From top to bottom, the parameters are $T_{\rm eff}$, log g, and [M/H]. The meanings of the red and green dots are the same as those explained in Figure 15. Blue dots and blue plus signs indicate spectra for which the log g derived by Ding2022 and this work are inconsistent, in the regions where the log g derived in this work is greater than 5.05 and less than 4.55, respectively. Orange dots indicate spectra with inconsistent log g between Ding2022 and this work in the region where the log g derived by Ding2022 is less than 4.35. The orange dots in Figure 23 have the same meaning as in this figure and will not be explained again. A small number of dM spectra have log g below 3.5 according to Ding2022, which are outside the range of the current figure. These spectra are marked as orange plus signs in Figure 23. A detailed discussion of these dots and plus signs is provided in Sections 4.2.2 and 4.3. The μ and σ in each panel represent the systematic difference and dispersion between the stellar parameters from different works, respectively.

trained model in Li2021 being influenced by erroneous APOGEE $T_{\rm eff}$ labels (red points), leading to systematic biases in the $T_{\rm eff}$ from Li2021. This hypothesis will be further examined in the temperature-color diagrams (Figures 24 and 25). At the metal-poor end, the [M/H] values from Li2021 are systematically lower than those from APOGEE with a larger dispersion. This could be attributed to a combination of incorrect labels and an imbalanced distribution of training data.

4. *Qiu2023*. Figure 20 displays comparisons of $T_{\rm eff}$, log g, [M/H], and [α/M] for gM stars between Qiu2023 and this work in the left column. The middle and right columns show comparisons between Qiu2023 and APOGEE, and this work and APOGEE, respectively. The systematic differences and dispersions between Qiu2023 and this work are 10 ± 32 K, 0.12 ± 0.26 dex, −0.00 ± 0.20 dex and −0.00 ± 0.09 dex, respectively. The $T_{\rm eff}$ from Qiu2023 and this work are generally consistent. Through an analysis similar to that in comparison 1, we find that the systematic structures in the other three parameters are likely caused by Qiu2023. These systematic structures may result from differences between the parameter labels in APOGEE DR16 and DR17, combined with the effects of different data-driven methods. Except for a small subset of spectra where APOGEE measures [α/M] in the range of $0.18 < [\alpha/M] < 0.24$ (marked with purple points), which are systematically underestimated in this work, the measurements from this work and APOGEE are largely consistent. This bias may be caused by an imbalance in the training data. For the purple points, Qiu2023 shows partial agreement with APOGEE, while the remaining cases exhibit an even more significant systematic underestimation.

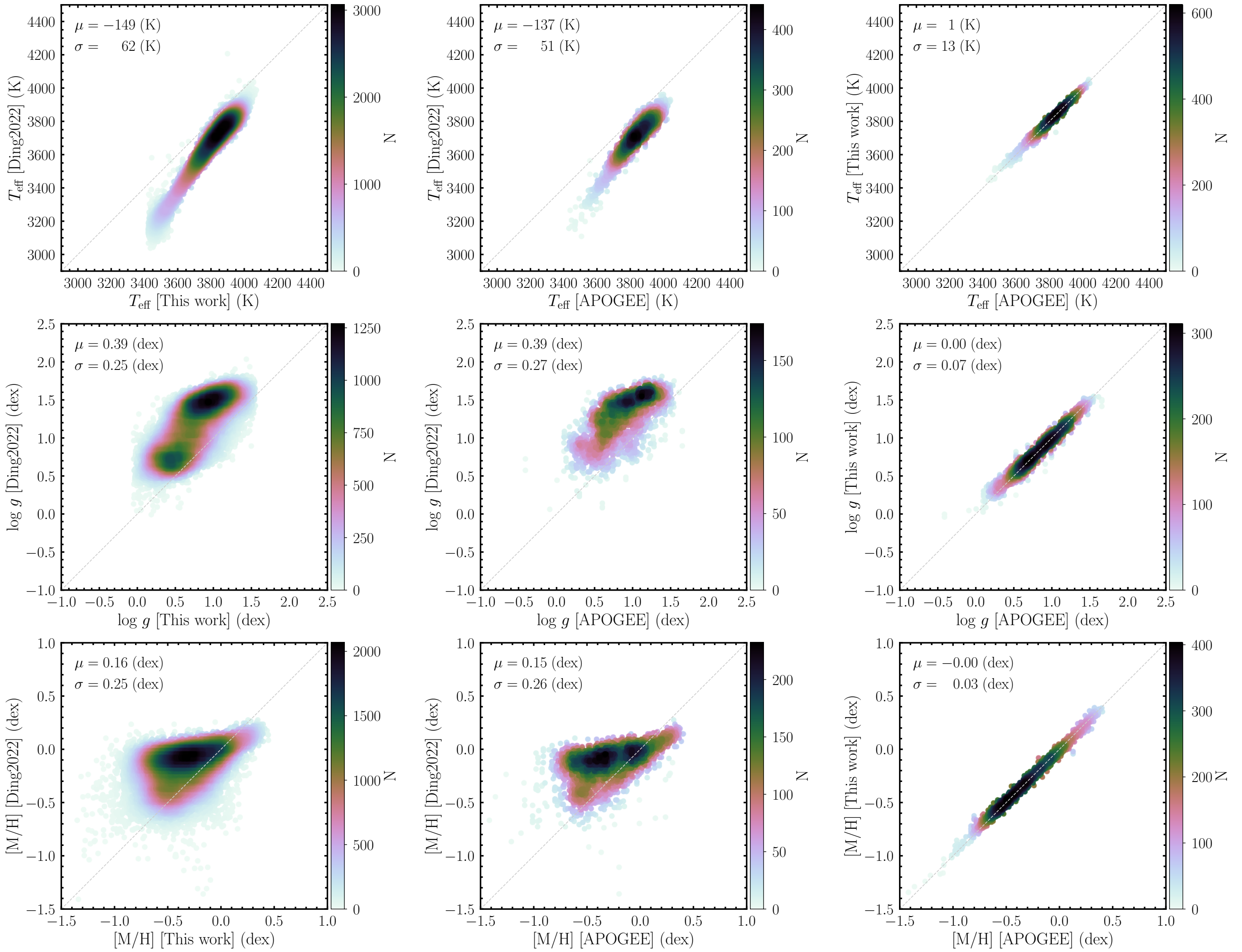

Figure 18. Comparison between the stellar parameters of gM stars derived in this work and those from Ding2022. The left, middle, and right columns show comparisons between Ding2022 and this work, Ding2022 and APOGEE, and this work and APOGEE, respectively. From top to bottom, the parameters are $T_{\rm eff}$, log g, and [M/H]. The μ and σ in each panel represent the systematic difference and dispersion between the stellar parameters from different works, respectively.

5. *Liang2022*. Figures 21 and 22 display comparisons of $T_{\rm eff}$, log g, and [M/H] for dM and gM stars between Liang2022 and this work in the left column. The middle and right columns show comparisons between Liang2022 and APOGEE, and this work and APOGEE, respectively. For dM stars, the systematic differences and dispersions between Liang2022 and this work are 0 ± 46 K, -0.04 ± 0.16 dex, and 0.01 ± 0.15 dex for $T_{\rm eff}$, log g, and [M/H], respectively. For gM stars, the corresponding values are 13 ± 45 K, 0.02 ± 0.14 dex, and 0.01 ± 0.15 dex. For both dM and gM stars, the three parameters measured by Liang2022 are largely consistent with those from this work, as well as with APOGEE. For dM stars, the log g from Liang2022 includes some outliers below 4.5 dex, and its [M/H] exhibits systematic structures. Using a similar analytical approach as in comparison 1, these issues are likely introduced by Liang2022. For gM stars, in comparison with APOGEE, the $T_{\rm eff}$, log g, and [M/H] from Liang2022 show greater dispersion than those from this work, which may be due to the limited precision of the photometric data.

Comparing each work to APOGEE, the stellar parameters provided in this work exhibit significant improvement in dispersion relative to the other five works. For dM stars, the dispersions in $T_{\rm eff}$, log g, and [M/H] obtained by other works were 41–69 K, 0.14–0.23 dex, and 0.11–0.32 dex, respectively, whereas this work achieves better dispersions of 31 K, 0.11 dex, and 0.08 dex. For gM stars, the dispersions in $T_{\rm eff}$, log g, and [M/H] derived by other works were 32–109 K, 0.15–0.31 dex (exceeding 0.25 dex in all studies except Liang2022), and 0.15–0.32 dex, while this work achieves better dispersions of 13 K, 0.07 dex, and 0.03 dex. Additionally, Qiu2023 reported an [α/M] dispersion of 0.07 dex, whereas this work achieves a dispersion of 0.02 dex. Overall, when comparing with APOGEE, the precision of parameters measured in this work improved by 21%–75% for dM stars and 53%–91% for gM stars, demonstrating that this approach substantially enhances the precision of parameter estimation for gM stars.

4.3. Isochrone

In Section 4.2.2, we analyzed the stellar parameters measured in this work, other studies, and APOGEE. The blue

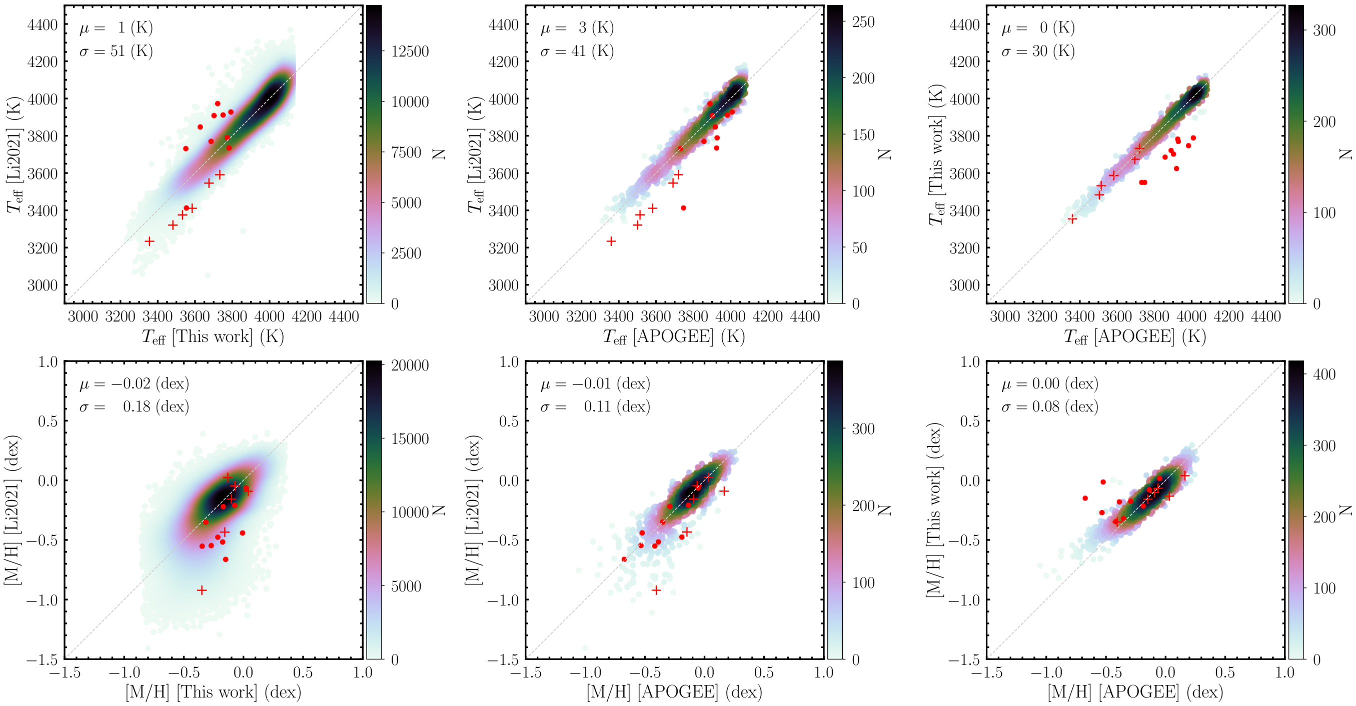

Figure 19. Comparison between the stellar parameters of dM stars derived in this work and those from Li2021. The left, middle, and right columns show comparisons between Li2021 and this work, Li2021 and APOGEE, and this work and APOGEE, respectively. From top to bottom, the parameters are $T_{\rm eff}$ and [M/H]. The meanings of the red dots are the same as those explained in Figure 15. Red plus signs indicate spectra for which the $T_{\rm eff}$ derived by Li2021 and APOGEE are inconsistent. The red plus signs in Figure 24 have the same meaning and will not be explained again. A detailed discussion of these dots and plus signs is provided in Sections 4.2.2 and 4.3. The μ and σ in each panel represent the systematic difference and dispersion between the stellar parameters from different works, respectively.

plus signs and points indicate spectra for which the log g from LASPM and Ding2022 are inconsistent with those from this work, corresponding to regions where log g in this work is either below 4.55 dex or above 5.05 dex. Previous analyses have demonstrated that the measurements in this work are more consistent with APOGEE, so no further analysis of the blue plus signs and points is necessary. The red points represent spectra for which the $T_{\rm eff}$ in this work are inconsistent with those from APOGEE, while the green points indicate spectra with discrepancies in log g. Based on earlier analyses, we preliminarily conclude that the stellar parameters measured by APOGEE for these red and green points may be problematic. To ensure a more rigorous analysis, we further examine these points using the Kiel diagram. The orange points and plus signs indicate spectra for which the log g measurements in Ding2022 and this work are inconsistent, corresponding to the regions where Ding2022 reported $3.5 <$ log $g < 4.35$ dex and log $g < 3.5$ dex, respectively. Since these spectra do not have corresponding APOGEE parameters, they also require further investigation using the Kiel diagram.

Figure 23 presents the Kiel diagrams of this work and the comparison studies. From top to bottom, the panels correspond to APOGEE, this work, Qiu2023, Ding2022, and LASPM. The gray lines represent 9 Gyr isochrones generated using the theoretical models from the Padova and Trieste Stellar Evolution Code (PARSEC; A. Bressan et al. 2012), with metallicities of −0.6, −0.3, 0, and 0.3 dex. It can be observed that the red and green points deviate from the isochrones in the Kiel diagram of APOGEE, whereas in the Kiel diagrams of this work, Ding2022, and LASPM, these points align more closely with the isochrones. This suggests that APOGEE likely encountered issues in the stellar parameter estimation for these red and green points. For the orange points, there is a trend of deviation from the isochrones in Ding2022's Kiel diagram, while in the Kiel diagrams of this work and LASPM, they align well with the isochrones, suggesting that Ding2022 likely made measurement errors. For the orange plus signs, they are located in the gM region in Ding2022's Kiel diagram, but in this work and LASPM's Kiel diagrams, they fall in the dM region and align with the isochrones. These spectra were manually checked and confirmed to be dMs, indicating that Ding2022 significantly misestimated the log g for some dM spectra. It is worth noting that, similar to Figure 16, the log g values measured by LASPM for gM stars in Figure 23 are concentrated around approximately 3, which differs significantly from the measurements obtained in this work and other studies. The possible reasons have been explained in comparison 1 of Section 4.2.2.

The Kiel diagram serves two purposes: (1) analyzing differences in stellar parameters between studies, and (2) evaluating metallicity gradients. It can be seen that, for both dM and gM stars, the metallicity gradients are more consistent between this work and APOGEE, following the trend of the isochrones. The metallicity gradient for dM stars is less pronounced, while for gM stars it is very clear. This may be due to the difficulty of achieving high-precision measurements within the narrow log g range of dM stars. To analyze the metallicity gradient of dM stars without the effect of log g, we have plotted the $T_{\rm eff}$ versus $(G_{\rm BP} - G_{\rm RP})_0$ diagram and the $T_{\rm eff}$ versus $({\rm W1} - {\rm W2})_0$ diagram for this work and the comparison studies in Figures 24 and 25. From top to bottom, the panels correspond to APOGEE, this work, Li2021, Ding2022, and LASPM. The PARSEC isochrones in Figures 24 and 25 are the same as those in Figure 23, and the

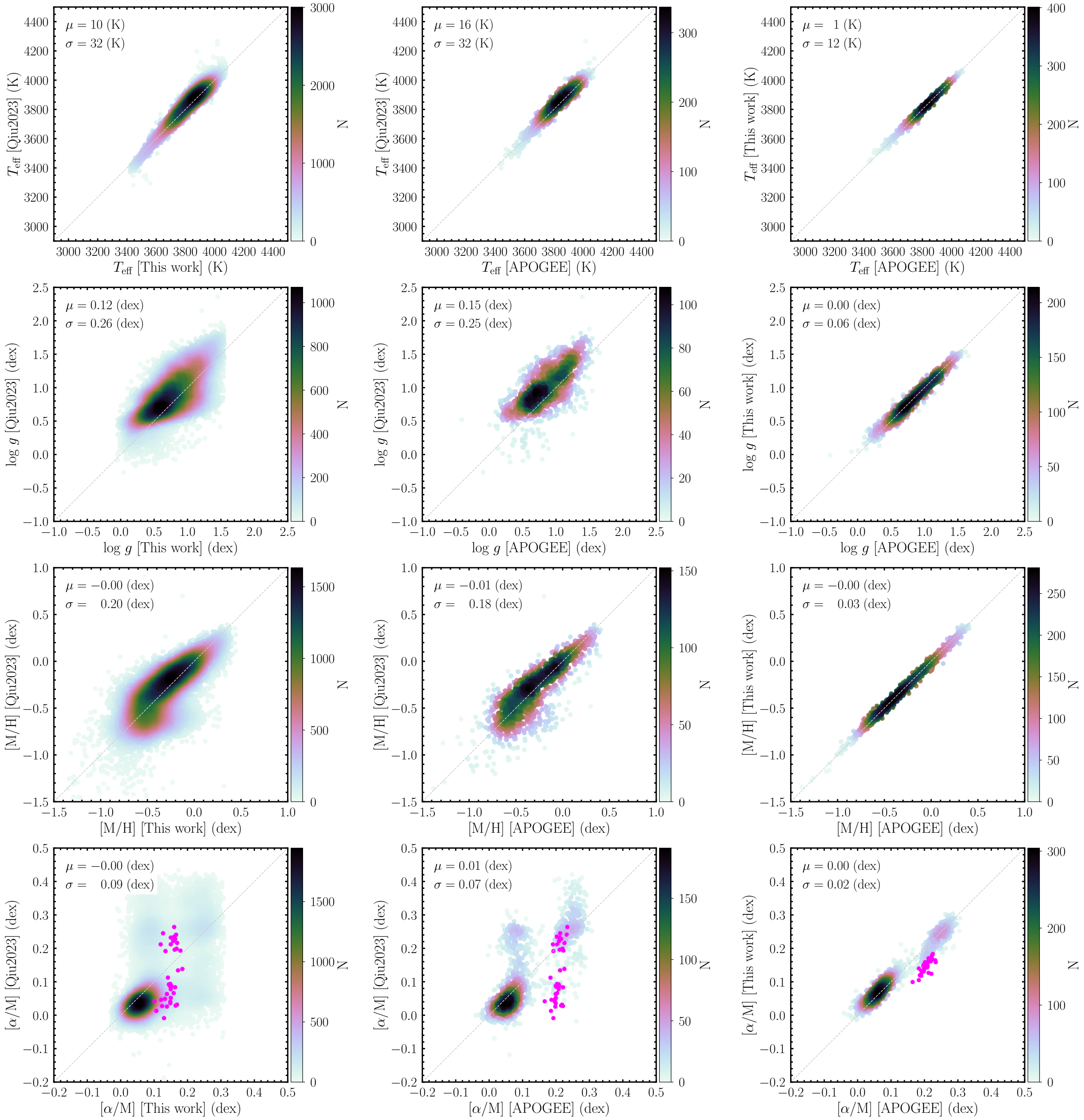

Figure 20. Comparison between the stellar parameters of gM stars derived in this work and those from Qiu2023. The left, middle, and right columns show comparisons between Qiu2023 and this work, Qiu2023 and APOGEE, and this work and APOGEE, respectively. From top to bottom, the parameters are $T_{\rm eff}$, log g, [M/H], and [α/M]. Purple dots indicate spectra for which the [α/M] derived in this work and by APOGEE are inconsistent. These points are discussed in Section 4.2.2. The μ and σ in each panel represent the systematic difference and dispersion between the stellar parameters from different works, respectively.

extinction correction and quality selection for $(G_{\rm BP} - G_{\rm RP})_0$ are the same as those described in Section 3.4.1. The W1 and W2 magnitudes are from the AllWISE catalog (R. M. Cutri et al. 2021; A. Bressan et al. 2012), and extinction corrections were applied. The $E(B - V)$ values come from the 3D dust map Bayestar19 (G. M. Green et al. 2019) mentioned in Section 3.4.1, with extinction coefficients from R. Zhang & H. Yuan (2023). To ensure the reliability of the W1 and W2 magnitudes, we only retained sources with W1 and W2 magnitude errors less than 0.03. From Figures 24 and 25, it can be seen that for the metallicity gradient of dM stars, this work is more consistent with APOGEE and shows a clearer trend, following the variation of the isochrones.

In the analysis in Section 4.2.2, the red plus signs indicate spectra for which the $T_{\rm eff}$ from Li2021 and APOGEE are inconsistent. It is preliminarily believed that the SLAM model trained by Li2021 was influenced by the incorrect labels from APOGEE (red points). Since Li2021 did not measure log g, this work can only use the $T_{\rm eff}$ versus $(G_{\rm BP} - G_{\rm RP})_0$ diagram (Figure 24) for further analysis. From Figure 24, it can be seen

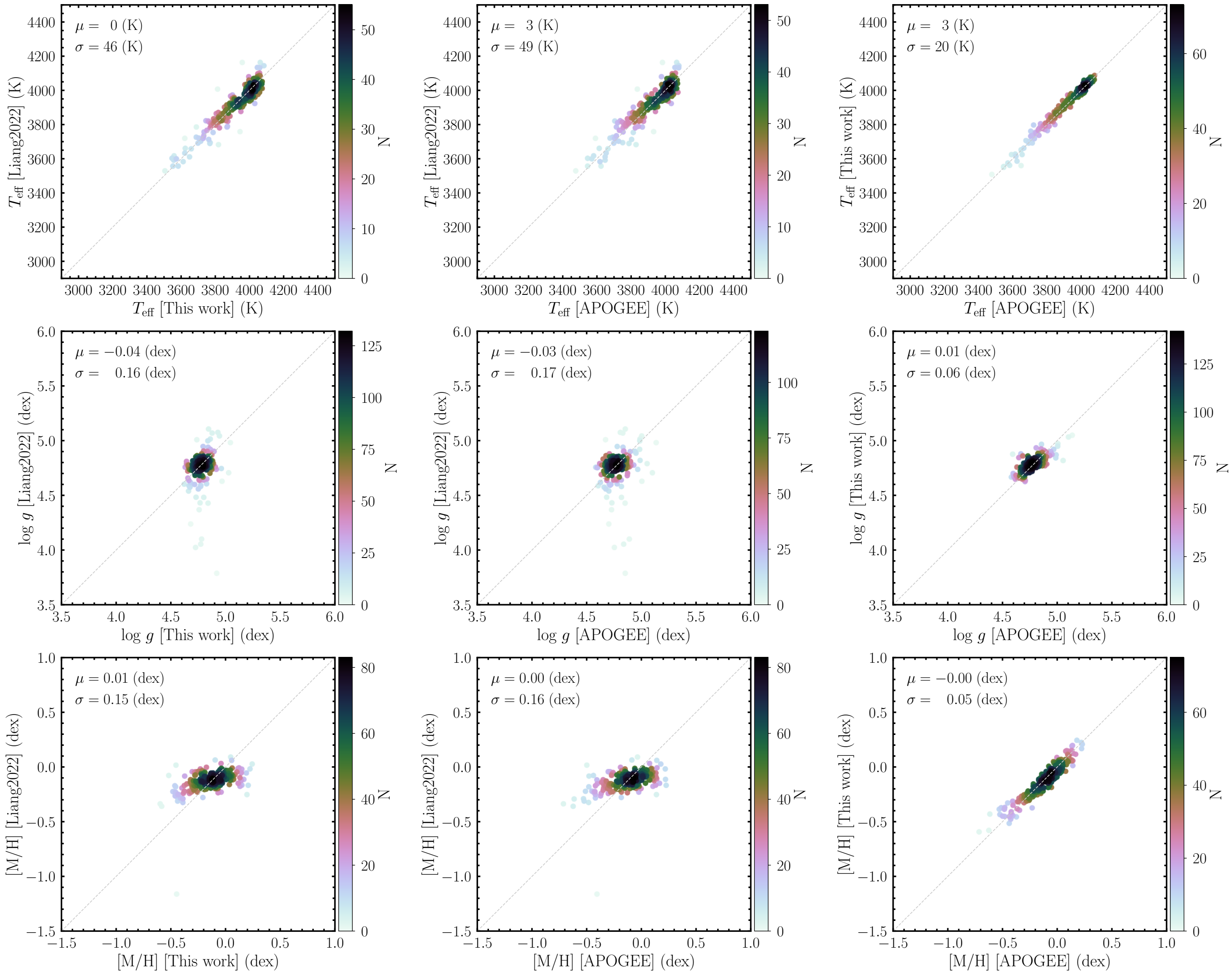

Figure 21. Comparison between the stellar parameters of dM stars derived in this work and those from Liang2022. The left, middle, and right columns show comparisons between Liang2022 and this work, Liang2022 and APOGEE, and this work and APOGEE, respectively. From top to bottom, the parameters are $T_{\rm eff}$, log g, and [M/H]. The μ and σ in each panel represent the systematic difference and dispersion between the stellar parameters from different works, respectively.

that the red points and plus signs are located in the anomalous region of Li2021's $T_{\rm eff}$ versus $(G_{\rm BP} - G_{\rm RP})_0$ diagram, while they are in the normal region in the $T_{\rm eff}$ versus $(G_{\rm BP} - G_{\rm RP})_0$ diagrams of this work, Ding2022, and LASPM. In APOGEE's $T_{\rm eff}$ versus $(G_{\rm BP} - G_{\rm RP})_0$ diagram, the red points are in the anomalous region, while the red plus signs are in the normal region. This further confirms that APOGEE made errors in the $T_{\rm eff}$ for the red points, which in turn affected the SLAM model trained by Li2021, leading to incorrect $T_{\rm eff}$ for the red points and plus signs in Li2021's results.

5. Summary

This work first designed and successfully implemented a fast and efficient process tailored to the characteristics of the vast amount of low-resolution LAMOST spectral data (see Figure 1). This process corrected the spectral types, dM and gM classifications, and RVs of the LAMOST DR10 M-type star catalog, ensuring the reliability of the corrections through manual verification, thereby constructing a cleaner M-type star sample. Second, we trained 10 CNN models for dM and gM spectra using tenfold cross-validation and model ensemble methods, predicting $T_{\rm eff}$, log g, [M/H], [α/M], and their associated errors. Finally, we conducted quality assessment cuts on the RVs and stellar parameters provided in this work and presented a recommended catalog (see Table 9). External comparisons confirm that the RVs and stellar parameters recommended in this work exhibit higher reliability. The main contributions of this work can be summarized as follows:

1. Identification and validation of non-M spectra. We trained two CNN classification models using LAMOST spectra and more accurate filtered classification labels (an eight-class model: OB, A, F, G, K, M, GALAXY and QSO, and a two-class model: WD and M) to classify all spectra in the LAMOST M-type star catalog, and by combining the positions of M-type stars in the Gaia CMD, we identified 22,496 non-M spectra after manual verification, of which 16,880 spectra have been updated in LAMOST DR8 and subsequent data releases.
2. Correction of dM and gM classifications. We trained a CNN model for dM/gM classification using LAMOST spectra and more accurate filtered classification labels to

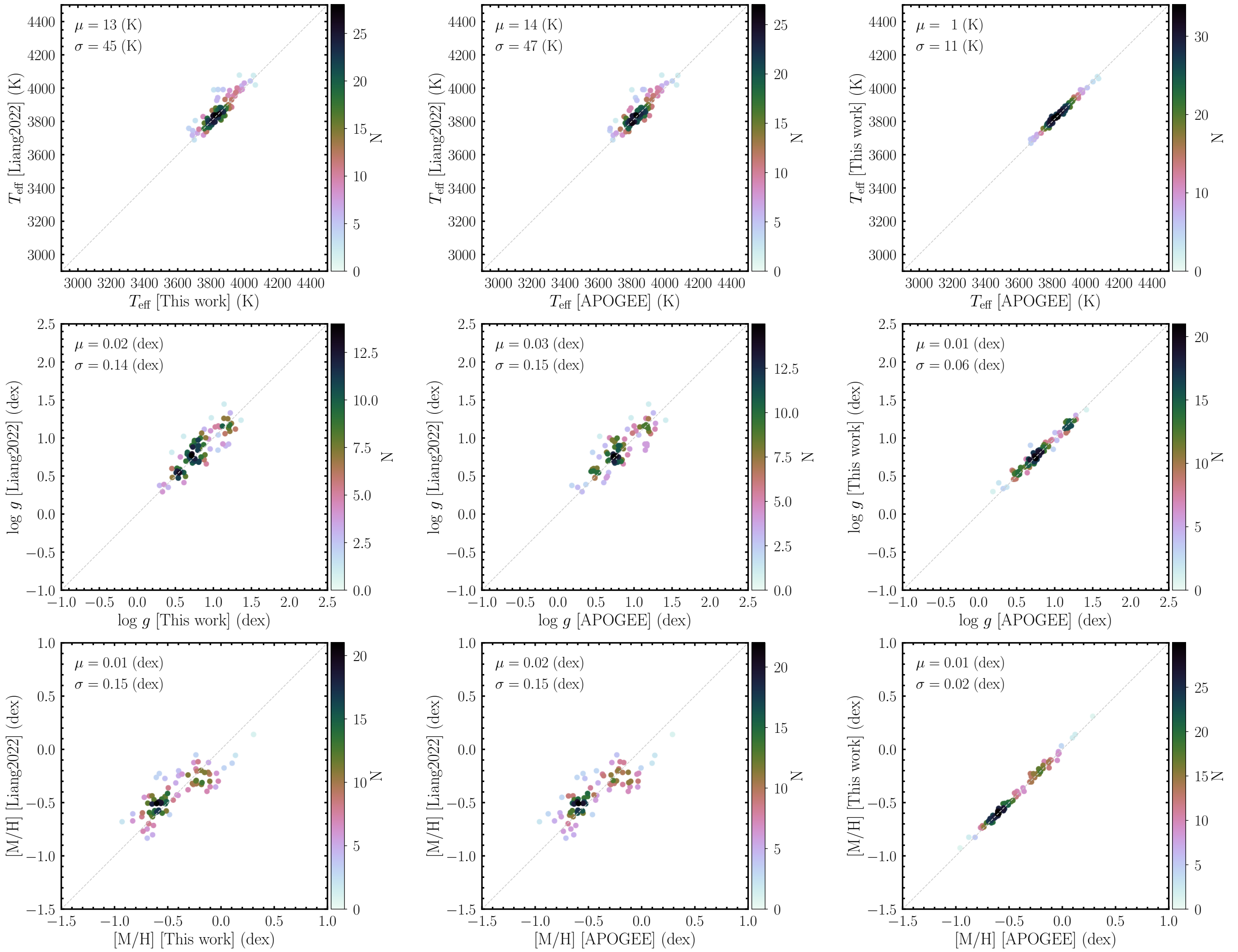

Figure 22. Comparison between the stellar parameters of gM stars derived in this work and those from Liang2022. The left, middle, and right columns show comparisons between Liang2022 and this work, Liang2022 and APOGEE, and this work and APOGEE, respectively. From top to bottom, the parameters are $T_{\rm eff}$, log g, and [M/H]. The μ and σ in each panel represent the systematic difference and dispersion between the stellar parameters from different works, respectively.

classify all M-type star spectra, and by combining the positions of dM and gM in the Gaia CMD and the dM/gM classification results provided by LAMOST, we manually corrected the dM/gM classification for 2078 spectra.

3. Correction of RVs for M-type stars. We remeasured the RVs of all M-type spectra using the TM and Doppler shift methods, calculating the corresponding errors. By comparing with the RVs from LAMOST, we manually checked the spectra with potentially incorrect LAMOST RVs and those with LAMOST $|\mathrm{RV}| > 150\,\mathrm{km\,s^{-1}}$, and corrected the RVs for 12,900 spectra. It is important to note that we have flagged 51,668 spectra with potential issues in the wavelength calibration lamps before 2012 January 14, as well as 89 spectra for which the RVs could not be determined due to spectral quality issues in the recommended catalog. The RVs of these spectra may be problematic and should be used with caution. The dispersion between the RVs recommended in this work and Gaia DR3 is $11\,\mathrm{km\,s^{-1}}$, which reduces to $7\,\mathrm{km\,s^{-1}}$ when the S/N is greater than 20. The systematic difference between the two is approximately $-5\,\mathrm{km\,s^{-1}}$, which is likely due to the wavelength calibration lamps used by LAMOST.
4. Measurement of M-type stellar parameters. We used a tenfold cross-validation approach to train 10 CNN regression models for dM and gM spectra, with stellar parameter labels from APOGEE DR16. The mean and standard deviation of the predictions from the 10 models were taken as the final stellar parameters and their associated errors. Using this model ensemble method, we predicted $T_{\rm eff}$, log g, [M/H], [α/M], and their errors for 820,493 dM spectra and 50,025 gM spectra. It is important to note that we performed rigorous quality assessment cuts of the stellar parameters (see Section 4.1) and flagged them in the recommended catalog. The number of recommended dM parameters is 716,207 (87% of the total dM spectra), and the number of recommended gM parameters is 40,907 (82% of the total gM spectra). For dM stars, the recommended

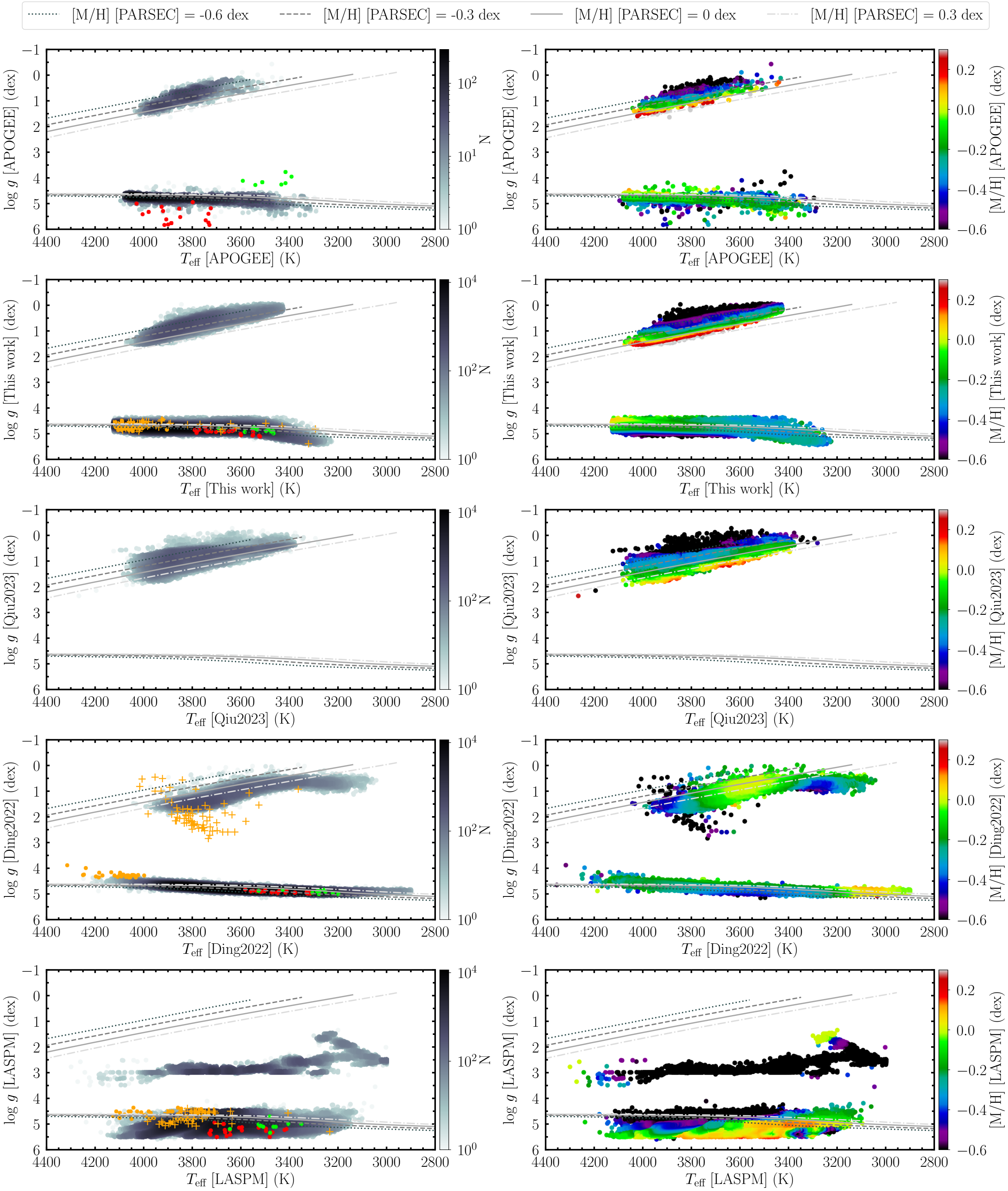

Figure 23. Kiel diagrams of this work and the comparison studies. From top to bottom, the panels show the Kiel diagrams from APOGEE, this work, Qiu2023, Ding2022, and LASPM. The meanings of the red and green dots in the left column are the same as those explained in Figure 15. The meanings of the orange dots and plus signs are the same as those explained in Figure 17. A detailed discussion of these dots and plus signs is provided in Sections 4.2.2 and 4.3. The gray lines in each panel represent 9 Gyr theoretical isochrones generated using the PARSEC (A. Bressan et al. 2012), with metallicities of −0.6, -0.3, 0.0, and 0.3 dex. The same PARSEC isochrone settings are adopted in Figures 24 and 25, and will not be described again.

stellar parameter ranges are 3225 K $< T_{\rm eff} <$ 4125 K, 4.35 dex $<$ log g $<$ 5.45 dex, -0.85 dex $<$ [M/H] $<$ 0.35 dex, and -0.13 dex $<$ [α/M] $<$ 0.25 dex; for gM stars, they are 3425 K $< T_{\rm eff} <$ 4075 K, -0.05 dex $<$ log g $<$ 1.55 dex, -1.35 dex $<$ [M/H] $<$ 0.45 dex, and -0.03 dex $<$ [α/M] $<$ 0.31 dex. For dM stars, the average internal errors for $T_{\rm eff}$, log g, [M/H], and [α/M] are 30 K, 0.07 dex, 0.07 dex, and 0.02 dex,

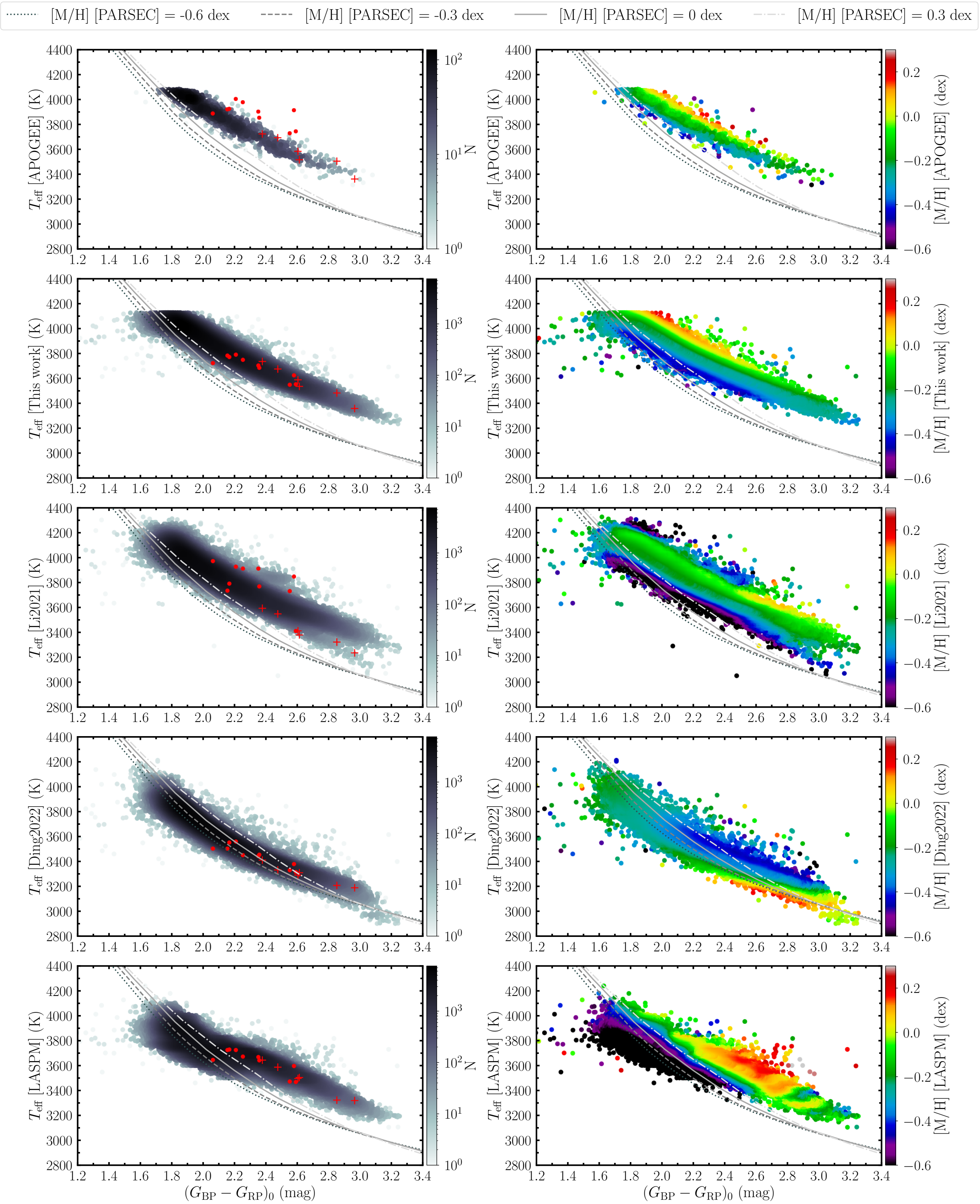

Figure 24. $T_{\rm eff}$ vs. $(G_{\rm BP} - G_{\rm RP})_0$ diagrams of dM stars from this work and the comparison studies. From top to bottom, the panels show the $T_{\rm eff}$ vs. $(G_{\rm BP} - G_{\rm RP})_0$ diagrams from APOGEE, this work, Li2021, Ding2022, and LASPM. The meanings of the red dots in the left column are the same as those explained in Figure 15. The meanings of the red plus signs are the same as those explained in Figure 19. A detailed discussion of these dots and plus signs is provided in Sections 4.2.2 and 4.3. The settings of the PARSEC isochrones (gray lines) shown in the panels are the same as those described in Figure 23.

respectively; for gM stars, they are 17 K, 0.07 dex, 0.05 dex, and 0.02 dex. For dM stars, the errors between this work and APOGEE DR16 are −0 ± 34 K, 0.00 ± 0.12 dex, 0.00 ± 0.09 dex, and 0.00 ± 0.03 dex; for gM stars, they are 1 ± 14 K, 0.00 ± 0.07 dex, 0.00 ± 0.04 dex, and 0.00 ± 0.02 dex.

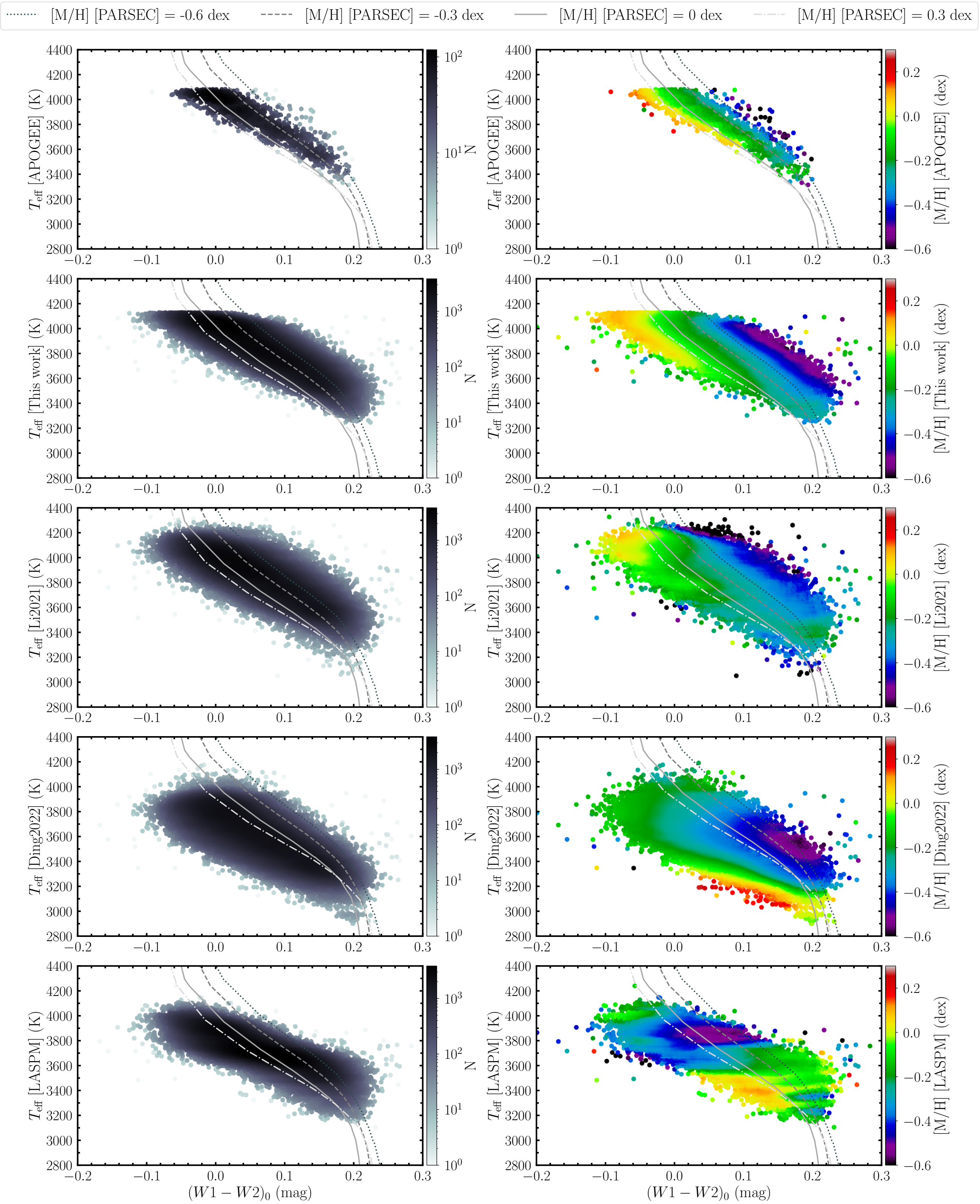

Figure 25. $T_{\rm eff}$ vs. $({\rm W1}-{\rm W2})_0$ diagrams of dM stars from this work and the comparison studies. From top to bottom, the panels show the $T_{\rm eff}$ vs. $({\rm W1}-{\rm W2})_0$ diagrams from APOGEE, this work, Li2021, Ding2022, and LASPM. The settings of the PARSEC isochrones (gray lines) shown in the panels are the same as those described in Figure 23.

5. Comparison of stellar parameters with other studies. First, this work used APOGEE results as a reference benchmark to evaluate the results of this work and five other M-type stellar parameter measurement studies. For dM stars, the precision of $T_{\rm eff}$, log g, and [M/H] measurements in this work shows improvements of 24%–55%, 21%–52%, and 27%–75% respectively compared to the other five studies; for gM stars, the precision of $T_{\rm eff}$, log g, [M/H], and [α/M] improves by 59%–88%, 53%–77%, 80%–91%, and 71% respectively.

> Compared to five previous studies, the parameters derived from this work demonstrate greater consistency with APOGEE while simultaneously achieving a remarkably significant improvement in parameter measurement precision for gM stars. Second, in the Kiel diagram, T_{eff} versus $(G_{\mathrm{BP}} - G_{\mathrm{RP}})_0$ diagram, and T_{eff} versus $(\mathrm{W1} - \mathrm{W2})_0$ diagram, the metallicity gradient of this work aligns more closely with APOGEE than the other five studies.

The advantages of the stellar parameters provided in this work are as follows: (1) The "label transfer + parameter prediction" strategy applied in this work, which used LAMOST spectra and high-precision APOGEE parameters as training samples, effectively reduces systematic errors arising from spectral mismatches compared to directly applying synthetic-trained models to observed spectra; compared to parameter inference methods, the "parameter prediction" method can provide more reliable parameter measurements with greater efficiency. (2) Compared to traditional machine learning algorithms, CNNs have superior feature extraction and nonlinear modeling capabilities, can effectively process high-dimensional data, and capture correlations between different parameters. (3) The tenfold cross-validated CNN ensemble architecture effectively reduces dependence on an individual data set and minimizes overfitting risks when training data is limited, enhancing both the reliability and stability of stellar parameter determinations.

The limitations of the stellar parameters provided in this work, using APOGEE as the reference benchmark, are as follows: (1) dM spectra in the range of $-1.1\,\mathrm{dex} < [\mathrm{M/H}] < -0.5\,\mathrm{dex}$ are systematically overestimated by approximately 0.1 dex. (2) dM spectra in the range of $[\alpha/\mathrm{M}] > 0.14\,\mathrm{dex}$ are systematically underestimated by approximately 0.1 dex. (3) gM spectra in the range of $0.18\,\mathrm{dex} < [\alpha/\mathrm{M}] < 0.24\,\mathrm{dex}$ are systematically underestimated by approximately 0.08 dex. These limitations are likely due to an imbalance in the training data in the above-mentioned parameter ranges. In the future, we will attempt to address the data imbalance issue using the following approaches: (1) Weight adjustment. During training, we can adjust the sample weights in the loss function to make the model more sensitive to less frequently occurring stellar parameter ranges. Weight adjustment helps the model focus more on regions with fewer samples, reducing bias. (2) Data augmentation. For relatively scarce stellar parameter samples, we can use specific data augmentation techniques, such as adding noise, oversampling, or using generative adversarial networks to generate missing samples, thus balancing the data and increasing its diversity.

Beyond the issues in stellar parameter measurements, the recommended catalog exhibits inherent constraints. (1) Despite implementing multiple criteria and conducting rigorous visual inspections of over 100,000 spectra to minimize contamination from non-M-type stars, the recommended catalog may still contain a small number of non-M spectra, mainly including low-quality UNKNOWN spectra and late K-type stars,[13] for which the DGCM, RVMM, and SPMM analyses may exhibit relatively larger uncertainties. (2) Since the recommended catalog is constructed based on the official LAMOST M-type star catalog, it is acknowledged that genuine M-type stars misclassified by the LAMOST pipeline as other spectral types may have been inadvertently excluded. Empirically, the misclassification rate of the LAMOST pipeline is estimated to be approximately 3%, which suggests that the recommended catalog encompasses the vast majority of M-type stars observed by LAMOST. Nevertheless, to ensure the construction of a more comprehensive and complete M-type star catalog, future systematic searches through the entire LAMOST data set will be necessary to identify and recover these potentially overlooked M-type candidates. (3) In constructing the recommended catalog, we excluded only the obvious spectral binaries identified during visual inspection within the SCM module, while the small fraction of spectral binaries present in the non-visually inspected spectra remained unfiltered. Additionally, we did not employ other criteria to specifically identify or exclude other types of binary systems. Although a known binary fraction for dM is probably relatively lower (J. G. Winters et al. 2019), the current parameter estimation methods may exhibit reduced accuracy when applied to binary spectra. To minimize the impact of binaries on parameter estimates, users can apply the `CMD_flag` = 1 filter in the recommended catalog to exclude potential binaries and sources with unreliable Gaia parameters.

In addition to the low-resolution observations, the LAMOST medium-resolution survey has released ∼10 million coadded spectra, with the official LAMOST catalog providing stellar parameters for only about one-quarter of the spectra. In the future, we will attempt to apply the methods proposed in this work to the stellar parameter measurements of M-type stars in LAMOST medium-resolution spectra.

Acknowledgments

We thank Zipeng Zheng, Rui Wang, Jingyi Zhang, Yanxin Guo, Bing Du, Xiao Kong, Fang Zuo, Kefei Wu, Wen Hou, Yihan Song, Xiaoting Fu, Mingyi Ding, Jiadong Li, B. Zhang, Peng Wei, Shuguo Ma, Yuanhao Wen, Xianglei Chen, and Caixia Qu for useful discussions. This work is supported by the National Natural Science Foundation of China (12273078, 12411530071, 12273075) and the National Astronomical Observatories of the Chinese Academy of Sciences (No. E4ZR0516). We also acknowledge support from the Royal Society IEC\NSFC\233140 exchange grant. Guoshoujing Telescope (LAMOST) is a National Major Scientific Project built by the Chinese Academy of Sciences. Funding for the Project has been provided by the National Development and Reform Commission. LAMOST is operated and managed by the National Astronomical Observatories, Chinese Academy of Sciences. This research makes use of data from the European Space Agency (ESA) mission Gaia, processed by the Gaia Data Processing and Analysis Consortium. Funding for the SDSS-IV has been provided by the Alfred P. Sloan Foundation, the US Department of Energy Office of Science, and the Participating Institutions. SDSS acknowledges support and resources from the Center for High-Performance Computing at the University of Utah. The SDSS website is at https://www.sdss.org/. This publication makes use of data products from the Wide-field Infrared Survey Explorer (WISE), which is a joint project of the University of California, Los Angeles, and the Jet Propulsion Laboratory/California Institute of

---

[13] Given the extreme similarity between the spectral features of late K-type and early M-type stars, reliable discrimination by both algorithm and visual inspection is difficult. Therefore, we roughly estimated the possible fraction of UNKNOWN spectra in the recommended catalog, which is approximately 0.8% (computed by 419/50,000; the two values were mentioned in Section 3.4.2), and based on our experience, we consider the fraction of late K-type contaminants to be roughly comparable in magnitude.

Technology, funded by the National Aeronautics and Space Administration.

This research also makes use of Astropy, a community-developed core Python package for Astronomy (Astropy Collaboration et al. 2013), the TOPCAT tool (M. B. Taylor 2005), and the VizieR catalog access tool and the SIMBAD database, operated at Centre de Donnees astronomiques de Strasbourg (CDS), France.

Facilities: LAMOST, Gaia, Sloan, WISE.

ORCID iDs

Shuo Li https://orcid.org/0000-0002-8913-3605
Yin-Bi Li https://orcid.org/0000-0001-7607-2666
A-Li Luo https://orcid.org/0000-0001-7865-2648
Jun-Chao Liang https://orcid.org/0009-0001-9085-8718
You-Fen Wang https://orcid.org/0000-0001-7671-4745
Jing Chen https://orcid.org/0000-0001-8869-653X
Shuo Zhang https://orcid.org/0000-0003-1454-1636
Mao-Sheng Xiang https://orcid.org/0000-0002-5818-8769
Hugh R. A. Jones https://orcid.org/0000-0003-0433-3665
Zhong-Rui Bai https://orcid.org/0000-0003-3884-5693
Xiao-Xiao Ma https://orcid.org/0000-0002-9279-2783
Yun-Jin Zhang https://orcid.org/0000-0001-7210-0666
Hai-Ling Lu https://orcid.org/0000-0002-8252-8743

References

Abdurro'uf, Accetta, K., Aerts, C., et al. 2022, ApJS, 259, 35
Allard, F., Homeier, D., & Freytag, B. 2011, ASPC, 448, 91
Astropy Collaboration, Robitaille, T. P., Tollerud, E. J., et al. 2013, A&A, 558, A33
Bailer-Jones, C. A. L., Rybizki, J., Fouesneau, M., Demleitner, M., & Andrae, R. 2021, AJ, 161, 147
Bello-García, A., Passegger, V. M., Ordieres-Meré, J., et al. 2023, A&A, 673, A105
Blanton, M. R., Bershady, M. A., Abolfathi, B., et al. 2017, AJ, 154, 28
Bochanski, J. J., Hawley, S. L., Covey, K. R., et al. 2010, AJ, 139, 2679
Boothroyd, A. I., & Sackmann, I. J. 1999, ApJ, 510, 232
Bressan, A., Marigo, P., Girardi, L., et al. 2012, MNRAS, 427, 127
Casagrande, L., & VandenBerg, D. A. 2018, MNRAS, 479, L102
Chen, J., Luo, A. L., Li, Y.-B., et al. 2022, ApJ, 931, 133
Cui, X.-Q., Zhao, Y.-H., Chu, Y.-Q., et al. 2012, RAA, 12, 1197
Cutri, R. M., Wright, E. L., Conrow, T., et al. 2021, yCat, II/328
De Angeli, F., Weiler, M., Montegriffo, P., et al. 2023, A&A, 674, A2
De Silva, G. M., Freeman, K. C., Bland-Hawthorn, J., et al. 2015, MNRAS, 449, 2604
Deng, L.-C., Newberg, H. J., Liu, C., et al. 2012, RAA, 12, 735
Ding, M.-Y., Shi, J.-R., Wu, Y., et al. 2022, ApJS, 260, 45
Du, B., Luo, A. L., Wang, S., et al. 2024, ApJS, 275, 42
Du, B., Luo, A. L., Zhang, S., et al. 2021, RAA, 21, 202
Eschen, Y. N. E., & Kunimoto, M. 2024, MNRAS, 531, 5053
Falcón-Barroso, J., Sánchez-Blázquez, P., Vazdekis, A., et al. 2011, A&A, 532, A95
Faria, J. P., Suárez Mascareño, A., Figueira, P., et al. 2022, A&A, 658, A115
Fouesneau, M., Frémat, Y., Andrae, R., et al. 2023, A&A, 674, A28
Gaia Collaboration, Creevey, O. L., Sarro, L. M., et al. 2023a, A&A, 674, A39
Gaia Collaboration, Prusti, T., de Bruijne, J. H. J., et al. 2016, A&A, 595, A1
Gaia Collaboration, Vallenari, A., Brown, A. G. A., et al. 2023b, A&A, 674, A1
García Pérez, A. E., Allende Prieto, C., Holtzman, J. A., et al. 2016, AJ, 151, 144
Gilmore, G., Randich, S., Asplund, M., et al. 2012, Msngr, 147, 25
Golovin, A., Reffert, S., Just, A., et al. 2023, A&A, 670, A19
Gray, R. O., & Corbally, J. C. 2009, Stellar Spectral Classification (Princeton Univ. Press)
Green, G. M., Schlafly, E., Zucker, C., Speagle, J. S., & Finkbeiner, D. 2019, ApJ, 887, 93
Grimm, S. L., Demory, B.-O., Gillon, M., et al. 2018, A&A, 613, A68
Gunn, J. E., Siegmund, W. A., Mannery, E. J., et al. 2006, AJ, 131, 2332
Guo, Y.-X., Yi, Z.-P., Luo, A. L., et al. 2015, RAA, 15, 1182
Husser, T. O., Wende-von Berg, S., Dreizler, S., et al. 2013, A&A, 553, A6
Ibata, R. A., Gilmore, G., & Irwin, M. J. 1994, Natur, 370, 194
Jofré, P., Heiter, U., & Soubiran, C. 2019, ARA&A, 57, 571
Jones, H. R. A., Pavlenko, Y., Lyubchik, Y., et al. 2023, MNRAS, 523, 1297
Jönsson, H., Holtzman, J. A., Allende Prieto, C., et al. 2020, AJ, 160, 120
Katz, D., Sartoretti, P., Guerrier, A., et al. 2023, A&A, 674, A5
Kingma, D. P., & Ba, J. 2014, arXiv:1412.6980
Kippenhahn, R., Weigert, A., & Weiss, A. 2013, Stellar Structure and Evolution (Springer)
Kirkpatrick, J. D., Kelly, D. M., Rieke, G. H., et al. 1993, ApJ, 402, 643
Kirkpatrick, J. D., & McCarthy, D. W. J. 1991, ApJS, 77, 417
Kossakowski, D., Kürster, M., Trifonov, T., et al. 2023, A&A, 670, A84
Kurucz, R. L. 2014, in Determination of Atmospheric Parameters of B, ed. E. Niemczura, B. Smalley, & W. Pych (Springer), 39
Laughlin, G., Bodenheimer, P., & Adams, F. C. 1997, ApJ, 482, 420
Li, J., Liu, C., Zhang, B., et al. 2021, ApJS, 253, 45
Li, J., Liu, C., Zhang, Z.-Y., et al. 2023, Natur, 613, 460
Li, J., Smith, M. C., Zhong, J., et al. 2016, ApJ, 823, 59
Liang, J., Bu, Y., Tan, K., et al. 2022, AJ, 163, 153
Liang, J.-C., Luo, A. L., Li, Y.-B., et al. 2024, ApJS, 275, 8
Lillo-Box, J., Figueira, P., Leleu, A., et al. 2020, A&A, 642, A121
Lindegren, L., Hernández, J., Bombrun, A., et al. 2018, A&A, 616, A2
Liu, C., Fu, J., Shi, J., et al. 2020, arXiv:2005.07210
Luo, A. L., Zhang, H.-T., Zhao, Y.-H., et al. 2012, RAA, 12, 1243
Luo, A. L., Zhao, Y.-H., Zhao, G., et al. 2015, RAA, 15, 1095
Majewski, S. R., Schiavon, R. P., Frinchaboy, P. M., et al. 2017, AJ, 154, 94
Mann, A. W., Feiden, G. A., Gaidos, E., Boyajian, T., & von Braun, K. 2015, ApJ, 804, 64
Mann, A. W., Gaidos, E., Lépine, S., & Hilton, E. J. 2012, ApJ, 753, 90
Marfil, E., Tabernero, H. M., Montes, D., et al. 2021, A&A, 656, A162
Mas-Buitrago, P., González-Marcos, A., Solano, E., et al. 2024, A&A, 687, A205
Passegger, V. M., Bello-García, A., Ordieres-Meré, J., et al. 2020, A&A, 642, A22
Passegger, V. M., Reiners, A., Jeffers, S. V., et al. 2018, A&A, 615, A6
Passegger, V. M., Schweitzer, A., Shulyak, D., et al. 2019, A&A, 627, A161
Paszke, A., Gross, S., Massa, F., et al. 2019, arXiv:1912.01703
Qiu, D., Tian, H., Li, J., et al. 2023, RAA, 23, 055008
Quirrenbach, A., CARMENES Consortium, Amado, P. J., et al. 2020, Proc. SPIE, 11447, 114473C
Rajpurohit, A. S., Allard, F., Rajpurohit, S., et al. 2018, A&A, 620, A180
Reid, I. N., & Gizis, J. E. 1997, AJ, 113, 2246
Shields, A. L., Ballard, S., & Johnson, J. A. 2016, PhR, 663, 1
Steinmetz, M., Zwitter, T., Siebert, A., et al. 2006, AJ, 132, 1645
Su, D.-Q., & Cui, X.-Q. 2004, ChJAA, 4, 1
Taylor, M. B. 2005, ASPC, 347, 29
Wang, S.-G., Su, D.-Q., Chu, Y.-Q., Cui, X., & Wang, Y.-N. 1996, ApOpt, 35, 5155
Wenger, M., Ochsenbein, F., Egret, D., et al. 2000, A&AS, 143, 9
West, A. A., Morgan, D. P., Bochanski, J. J., et al. 2011, AJ, 141, 97
Winters, J. G., Henry, T. J., Jao, W.-C., et al. 2019, AJ, 157, 216
Yang, C., Xue, X.-X., Li, J., et al. 2019, ApJ, 886, 154
Yanny, B., Rockosi, C., Newberg, H. J., et al. 2009, AJ, 137, 4377
York, D. G., Adelman, J., Anderson, J. E. J., et al. 2000, AJ, 120, 1579
Zhang, R., & Yuan, H. 2023, ApJS, 264, 14
Zhang, S., Luo, A. L., Comte, G., et al. 2019, ApJS, 240, 31
Zhang, S., Luo, A. L., Comte, G., et al. 2021, ApJ, 908, 131
Zhang, S., Zhang, H.-W., Ting, Y.-S., et al. 2025, ApJS, 277, 47
Zhao, G., Zhao, Y.-H., Chu, Y.-Q., Jing, Y.-P., & Deng, L.-C. 2012, RAA, 12, 723
Zheng, Z.-P., Qiu, B., Luo, A. L., & Li, Y.-B. 2020, PASP, 132, 024504
Zhong, J., Lépine, S., Hou, J., et al. 2015a, AJ, 150, 42
Zhong, J., Lépine, S., Li, J., Chen, L., & Hou, J. 2016, IAUS, 317, 371
Zhong, J., Lépine, S., Li, J., et al. 2015b, RAA, 15, 1154